

MTS-JEPA: Multi-Resolution Joint-Embedding Predictive Architecture for Time-Series Anomaly Prediction

Yanan He¹ Yunshi Wen² Xin Wang³
Tengfei Ma³

Abstract

Multivariate time series underpin modern critical infrastructure, making the prediction of anomalies a vital necessity for proactive risk mitigation. While Joint-Embedding Predictive Architectures (JEPA) offer a promising framework for modeling the latent evolution of these systems, their application is hindered by representation collapse and an inability to capture precursor signals across varying temporal scales. To address these limitations, we propose MTS-JEPA, a specialized architecture that integrates a multi-resolution predictive objective with a soft codebook bottleneck. This design explicitly decouples transient shocks from long-term trends, and utilizes the codebook to capture discrete regime transitions. Notably, we find this constraint also acts as an intrinsic regularizer to ensure optimization stability. Empirical evaluations on standard benchmarks confirm that our approach effectively prevents degenerate solutions and achieves state-of-the-art performance under the early-warning protocol.

1. Introduction

Multivariate time series constitute the backbone of modern critical infrastructure. These systems range from industrial manufacturing to server operations. Within such complex environments, the primary objective extends beyond mere observation. The goal is to anticipate risks before they manifest as catastrophic failures. We focus on this task of anomaly prediction. This differs fundamentally from standard anomaly detection and forecasting (Park et al., 2025). Detection is inherently reactive and identifies faults only after their occurrence (Ruff et al., 2018; Xu et al., 2022). Forecasting typically regresses numerical values and

¹ Purdue University, West Lafayette, IN, USA ² Rensselaer Polytechnic Institute, Troy, NY, USA ³ Stony Brook University, Stony Brook, NY, USA . Correspondence to: Tengfei Ma <tengfei.ma@stonybrook.edu>.

Preprint. February 5, 2026.

is prone to high-frequency noise (Zhou et al., 2021). In contrast, anomaly prediction (Jhin et al., 2023; Zhao et al., 2024) aims to capture precursor patterns indicative of future instability. However, achieving this is non-trivial. Real-world data is characterized by stochastic volatility that often obscures early warning signals. Many existing methods still rely heavily on point-wise reconstruction or regression. This tendency risks overfitting to unpredictable fluctuations. It underscores the need for a paradigm that effectively models high-level system dynamics rather than raw data points.

Motivated by this need, predictive world models have emerged to reason about the underlying evolution of an environment. Joint-Embedding Predictive Architectures (JEPA) represent a significant advancement in this direction (As-sran et al., 2023). The core principle involves predicting missing information within an abstract latent space rather than reconstructing raw input signals. This design forces the model to capture high-level state transitions while ignoring unpredictable details. Such a mechanism naturally aligns with multivariate time series, where stochastic volatility often masks the true evolution of system states. Consequently, representation-space predictive modeling offers a robust pathway for identifying early warning signals compared to precise numerical regression. While preliminary adaptations to time series exist (Ennadir et al., 2025), the stability and failure modes of JEPA objectives in this continuous domain remain poorly understood.

Concretely, this deficiency manifests as two primary challenges. The first is representation collapse, a phenomenon intrinsic to the self-distillation objective of latent-space prediction. In the absence of negative samples, the optimization landscape admits a degenerate solution where the encoder maps diverse inputs to a constant vector. Theoretical analysis confirms that this effectively reduces the embedding covariance rank to zero (Chen & He, 2021; Tian et al., 2021), yielding a vanishing training loss but a feature space devoid of discriminative information. The second challenge involves the multi-scale nature of anomaly precursors. As illustrated in Figure 1a, standard JEPA architectures operate at a fixed temporal granularity. However, anomalous signals in real-world systems are rarely confined to a sin-

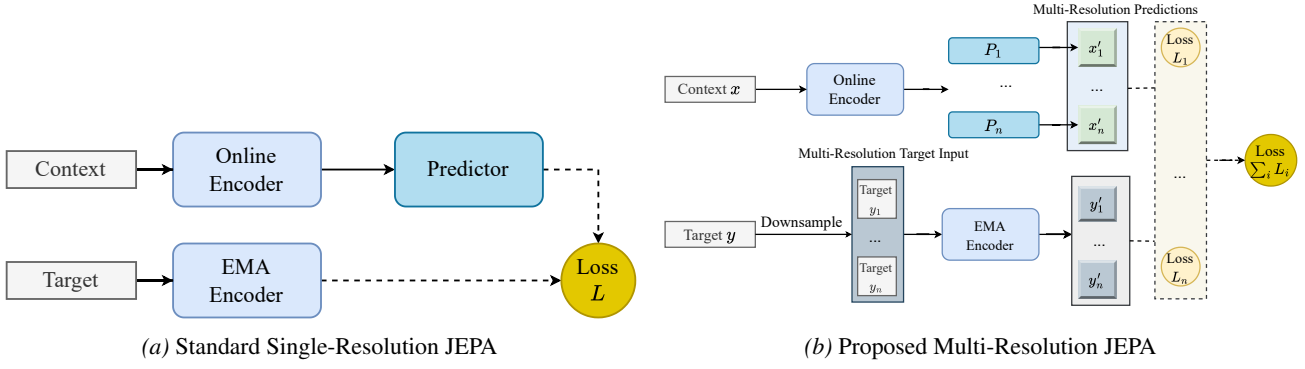


Figure 1. Comparison between standard single-resolution JEPA (A) and the proposed multi-resolution JEPA (B).

gle sampling rate. They often manifest as precursors distributed across distinct frequency bands or temporal resolutions (Wang et al., 2024; Liu et al., 2022a). Therefore, a single-resolution model inevitably fails to capture dynamics that evolve outside its specific observational scale.

To address these limitations, we propose the **Multi-resolution Time-Series JEPA** (MTS-JEPA). First, we employ a multi-resolution predictive objective. Unlike single-scale models (Figure 1a), our parallel latent pathways explicitly capture multi-scale dynamics, spanning both transient shocks and evolving trends (Figure 1b). Second, we incorporate a soft codebook bottleneck (Van Den Oord et al., 2017; Gong et al., 2019). We adopt this discrete structure primarily to suit anomaly prediction, as it compels the model to capture temporal evolution as definable regime transitions rather than unstructured drift. Meanwhile, we observe and demonstrate that this design yields a vital secondary benefit: it acts as an intrinsic regularizer, mitigating representation collapse without explicit negative sampling. Together, they make MTS-JEPA more suitable and stable for anomaly prediction.

In summary, our main contributions are:

- **World Model for Anomaly Prediction:** We formulate time-series anomaly prediction as representation-space predictive modeling with JEPA-style targets, and show that modeling latent evolution is well suited for early warning.
- **Multi-Resolution JEPA:** We propose the first multi-resolution architecture within the JEPA framework for time-series. This novel design enables the model to capture scale-variant precursors, ranging from sudden shocks to slow drifts, which single-resolution baselines fail to detect.
- **Soft Codebook Bottleneck:** We introduce differentiable quantization to enforce a discrete inductive bias, sharpening the distinction between normal patterns and structural

anomalies. Furthermore, this constraint naturally stabilizes the optimization landscape and prevents representation collapse, ensuring the predictor learns meaningful semantic transitions rather than converging toward trivial, degenerate solutions.

2. Related Works

Anomaly Prediction. Time-series research has largely followed two directions: forecasting and detection. Forecasting approaches primarily learn trajectory regression objectives (Zhou et al., 2021; Liu et al., 2024) and are typically evaluated on value prediction accuracy rather than early-warning separability. In contrast, detection methods score the current window and are benchmarked under reactive protocols (Ruff et al., 2018; Xu et al., 2022). Consequently, there is growing interest in moving beyond reactive detection toward early-warning settings, where the goal is to anticipate future abnormality or failure risk ahead of time (Jhin et al., 2023; Zhao et al., 2024; Park et al., 2025). However, many existing formulations remain tied to input-space objectives or detector adaptations, suggesting the value of exploring representation-space predictive models that emphasize latent dynamics over local noise, especially when precursors unfold across multiple time horizons. Another line of work related to our method is vector-quantized (VQ) representation learning (Van Den Oord et al., 2017), which has been adapted for time-series anomaly detection (Lee et al., 2023; 2024; Wen et al., 2025); however, our method differs essentially in the target task, representation granularity, and predictive framework.

Joint Embedding Predictive Architectures. Self-supervised learning for time series is often built on masked modeling, as in PatchTST (Nie et al., 2023), or contrastive learning over augmented views, as in TS2Vec (Yue et al., 2022). In parallel, Joint-Embedding Predictive Architectures (JEPA) formulate predictive world models by forecasting future representations directly in latent

space, as demonstrated by I-JEPA for images and V-JEPA for videos (Assran et al., 2023; Bardes et al., 2024). By emphasizing latent predictability, JEPA encourages higher-level, state-like representations, which aligns naturally with time series as noisy observations of underlying evolving processes. Recent efforts have begun to adapt JEPA to time series, including TS-JEPA (Ennadir et al., 2025). However, JEPA-style predictive world models remain less explored for complex time-series systems, and stabilizing latent-space self-distillation objectives on continuous, non-stationary time series remains practically challenging.

Multi-Scale Dynamics. Multi-resolution modeling is widely used in representation learning to capture both global context and local detail, especially in computer vision (Lin et al., 2017). Time series share a similar multi-scale nature, where long-term trends coexist with fast local variations. Recent time-series models such as Pyraformer (Liu et al., 2022b) and TimeMixer (Wang et al., 2024) incorporate multi-scale structure through pyramid-style attention or multi-granularity mixing. In most cases, scale is introduced to improve forecasting accuracy or efficiency, rather than to explicitly model state evolution at multiple temporal rates. A less explored direction is to incorporate multi-scale structure into predictive world models, so that latent states can be propagated across different time scales. This perspective is particularly relevant for anomaly prediction, where early signs may appear as slow drift or short-lived shocks. These observations point to multi-scale latent dynamics as a natural ingredient for early warning.

3. Method

3.1. Problem Setup

Consider a multivariate time series $\mathbf{x} \in \mathbb{R}^{T \times V}$. We partition \mathbf{x} into a sequence of non-overlapping windows $\{\mathbf{W}_t\}_{t=1}^N$, where each window $\mathbf{W}_t \in \mathbb{R}^{T_w \times V}$ contains T_w time steps. Our goal is to learn a representation from the current window \mathbf{W}_t to anticipate the anomaly status of the subsequent window \mathbf{W}_{t+1} , enabling proactive intervention by forecasting whether the next window will be anomalous.

Framework Overview. This proactive setting is difficult in practice because precursor cues are often weak, non-stationary, and may emerge at different temporal scales, making stable self-supervised prediction nontrivial. We propose a new JEPA framework to solve this challenging task. (1) To expose such scale-variant precursors, we construct dual-resolution inputs that disentangle local volatilities from global trends, described next in Section 3.2. As illustrated in Figure 2, MTS-JEPA then adopts an asymmetric teacher–student design: an online context branch predicts future latent states from the current window, while a

momentum-updated target branch provides supervision. The asymmetry imposes a deliberate information gap: the online branch observes only the fine-grained view, yet is supervised to match multi-scale targets produced from both fine and coarse views, encouraging scale-aware representations. (2) In addition, a soft codebook bottleneck is introduced to impose a discrete inductive bias for anomaly prediction by mapping continuous features to prototype-anchored code distributions, as formalized in Section 3.3.

3.2. Input Formulation and Multi-Scale Views

To make scale-variant precursor patterns learnable under a unified predictive objective, we build dual-scale views from each raw window. We first apply RevIN (Kim et al., 2022) to \mathbf{W}_t , yielding the normalized window $\hat{\mathbf{W}}_t$. The affine statistics are cached to invert normalization for the reconstruction loss. We then construct two views at different resolutions:

Fine View (Patching). We tokenize $\hat{\mathbf{W}}_t$ into P patches of length L (where $T_w = P \cdot L$), forming the fine-grained representation:

$$\mathbf{X}_t^{\text{fine}} = \text{Patch}(\hat{\mathbf{W}}_t) \in \mathbb{R}^{P \times L \times V}. \quad (1)$$

Coarse View (Downsampling). Simultaneously, we generate a global view by averaging every P time points (Appendix A.2) to capture low-frequency trends. The resulting sequence of length L is treated as a single patch, aligning its dimensionality with the patch-based format:

$$\mathbf{X}_t^{\text{coarse}} = \text{DownAvg}_P(\hat{\mathbf{W}}_t) \in \mathbb{R}^{1 \times L \times V}. \quad (2)$$

The Online Branch processes only $\mathbf{X}_t^{\text{fine}}$, while the Target Branch encodes both resolutions at $t+1$ for supervision. This asymmetry serves as a structural inductive bias, compelling the model to encapsulate multi-scale semantics. Consequently, to bridge this deliberate information gap, we next detail the architectural machinery constructed to orchestrate the flow from partial local observations to stable global predictions.

3.3. Architecture

MTS-JEPA couples a shared encoder, a soft codebook, a dual-resolution predictor, and an auxiliary decoder.

Encoder. Weak and scale-variant precursors call for representations that are predictable and comparable across resolutions. We therefore use a shared encoder \mathcal{E} to embed raw windows into a compact latent space, using a channel-independent input formulation. Implemented as a residual CNN tokenizer followed by a Transformer backbone, \mathcal{E} supports variable-length inputs, so both fine-grained patch

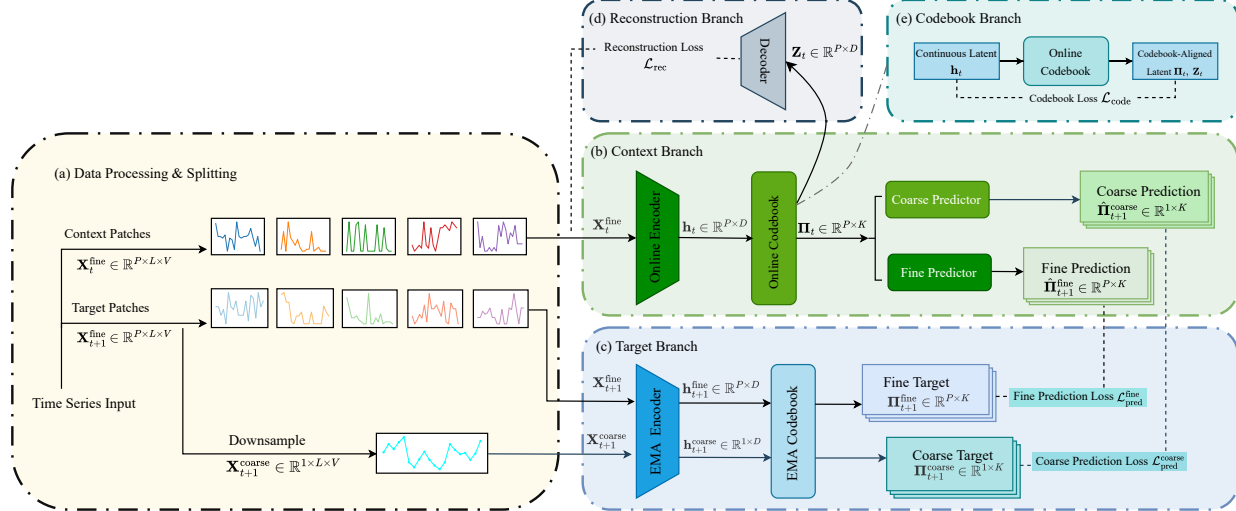


Figure 2. Overview of the MTS-JEPA framework for time series representation learning.

sequences and a single coarse-grained token are processed with the same parameters. Thus, a single encoder maps both resolutions into the same embedding space.

- (i) **Online encoder (\mathcal{E}_θ):** $\mathbf{h}_t = \mathcal{E}_\theta(\mathbf{X}_t^{\text{fine}})$. Operating under partial observation, \mathcal{E}_θ receives only the fine-grained view. It is trained to align with targets produced from both fine and coarse views (via the momentum teacher), which pressures the online representation to internalize global context from local evidence.
- (ii) **EMA encoder (\mathcal{E}_ξ):** A momentum-updated copy of the online encoder with holistic visibility. It processes both fine and coarse views to generate comprehensive, multi-scale targets: $\mathbf{h}_{t+1}^{\text{fine}} = \mathcal{E}_\xi(\mathbf{X}_{t+1}^{\text{fine}})$ and $\mathbf{h}_{t+1}^{\text{coarse}} = \mathcal{E}_\xi(\mathbf{X}_{t+1}^{\text{coarse}})$.

However, continuous encoder features often entangle nuisance variations. To mitigate this, we introduce a soft codebook that projects features onto a finite set of prototypes. This discretization not only captures regime-like patterns but also imposes an explicit geometric constraint on the latent space, which, as we detail next, is crucial for ensuring both representation stability and expressiveness.

Codebook. Formally, we implement this projection via a differentiable bottleneck \mathcal{Q} that maps continuous encoder features into a finite set of learnable prototypes $\{\mathbf{c}_k\}_{k=1}^K \subset \mathbb{R}^D$. For each patch representation $\mathbf{h}_{t,i} \in \mathbb{R}^D$, \mathcal{Q} outputs a soft code distribution $\mathbf{p}_{t,i} \in \Delta^{K-1}$, where $\Delta^{K-1} := \{\mathbf{p} \in \mathbb{R}^K : \mathbf{p} \succeq 0, \mathbf{1}^\top \mathbf{p} = 1\}$. We parameterize $\mathbf{p}_{t,i}$ via

temperature-scaled cosine similarity:

$$p_{t,i,k} = \frac{\exp\{\langle \bar{\mathbf{h}}_{t,i}, \bar{\mathbf{c}}_k \rangle / \tau\}}{\sum_{j=1}^K \exp\{\langle \bar{\mathbf{h}}_{t,i}, \bar{\mathbf{c}}_j \rangle / \tau\}}, \quad (3)$$

where $\bar{\mathbf{h}}_{t,i}$ and $\bar{\mathbf{c}}_k$ denote ℓ_2 -normalized vectors. We stack these patch-wise distributions to form the window-level code sequence $\mathbf{\Pi}_t := [\mathbf{p}_{t,1}; \dots; \mathbf{p}_{t,P}] \in \mathbb{R}^{P \times K}$, which serves as the predictor input. In parallel, we compute the expected code embedding $\mathbf{z}_{t,i} := \sum_{k=1}^K p_{t,i,k} \mathbf{c}_k \in \mathbb{R}^D$, which is used by the auxiliary decoder for reconstruction.

Since $\mathbf{p}_{t,i} \in \Delta^{K-1}$, the soft embedding $\mathbf{z}_{t,i} = \sum_k p_{t,i,k} \mathbf{c}_k$ constitutes a convex combination of finitely many prototypes and therefore remains within the bounded convex hull of $\{\mathbf{c}_k\}$. This boundedness provides an explicit geometric constraint on the latent space, preventing unbounded feature excursions and improving score stability; a formal **upper bound** is given in Appendix A.3.1. Complementarily, Appendix A.3.2 derives a strictly positive **lower bound** on the batch variance, i.e., $\text{Tr}(\text{Cov}(\mathbf{z})) > 0$, providing a sufficient non-collapse certificate. Together, these bounds ensure that $\mathbf{\Pi}_t$ provides a compact, regime-level description of the window that is both stable and expressive.

Predictor. With the latent dynamics discretized into a stable code sequence $\mathbf{\Pi}_t$, the remaining challenge is to forecast the system's evolution. Recognizing that anomalies often originate from conflicting temporal scales, we employ a dual-branch predictor to explicitly decouple these dynamics. Both branches operate on the same history $\mathbf{\Pi}_t$ but target distinct future resolutions:

- (i) **Fine Predictor (Micro-Dynamics):** To capture high-frequency volatility and local point anomalies, a

Transformer maps Π_t to a sequence of fine-grained predictions $\hat{\Pi}_{t+1}^{\text{fine}} \in \mathbb{R}^{P \times K}$. This branch preserves the patch-wise resolution, ensuring that transient disturbances are not smoothed out.

(ii) **Coarse Predictor (Macro-Dynamics):** To distill low-frequency trends and global distribution shifts, a learnable query token \mathbf{q} aggregates the entire history into a single global prediction $\hat{\Pi}_{t+1}^{\text{coarse}} \in \mathbb{R}^{1 \times K}$ via cross-attention:

$$\hat{\Pi}_{t+1}^{\text{coarse}} = \text{CrossAttn}(\mathbf{q}, \Pi_t). \quad (4)$$

This mechanism forces the model to abstract away local noise and focus on the trajectory of the system state.

For supervision, the EMA branch generates the corresponding multi-scale targets Π_{t+1}^{fine} and $\Pi_{t+1}^{\text{coarse}}$ using the shared codebook \mathcal{Q} .

Decoder. Because prediction alone can encourage overly abstract codes, an auxiliary decoder \mathcal{D} reconstructs the input patches $\mathbf{X}_t^{\text{fine}}$ from the online soft-quantized embeddings \mathbf{z}_t to retain signal-level semantics. The reconstruction is evaluated after inverting RevIN using the cached statistics.

MTS-JEPA achieves proactive anomaly prediction via multi-resolution forecasting of regime-level dynamics from the current window. We next formalize the unified training objective in Section 3.4.

3.4. Optimization Objective

We first introduce the notation used to define the three coupled objectives. Let $\mathbf{p}_{t,i} \in \mathbb{R}^K$ denote the online soft code distribution for patch i at window t (Eq. 3), satisfying $\mathbf{p}_{t,i} \geq \mathbf{0}$ and $\mathbf{1}^\top \mathbf{p}_{t,i} = 1$. Let $\mathbf{z}_{t,i} = \sum_{k=1}^K p_{t,i,k} \mathbf{c}_k$ be the corresponding soft-quantized latent. The fine predictor outputs $\hat{\mathbf{p}}_{t+1,i}^{\text{fine}}$ and latent $\hat{\mathbf{z}}_{t+1,i}$ for each patch, while the coarse predictor outputs a single distribution $\hat{\mathbf{p}}_{t+1}^{\text{coarse}}$. All targets $\mathbf{p}_{t+1,i}^{\text{fine}}$, $\mathbf{p}_{t+1}^{\text{coarse}}$ and $\mathbf{z}_{t+1,i}$ are produced by the EMA (target) branch.

Overall objective. We optimize the online encoder, codebook, predictors, and decoder using three terms:

$$\mathcal{L} = \mathcal{L}_{\text{pred}} + \mathcal{L}_{\text{code}} + \lambda_r \mathcal{L}_{\text{rec}}. \quad (5)$$

With the overall objective in place, we detail each term next.

(A) Predictive Objective ($\mathcal{L}_{\text{pred}}$). We supervise online predictions using EMA targets at both fine (patch) and coarse (window) resolutions, so that the representation is jointly shaped by local precursors and global trends.

$$\mathcal{L}_{\text{pred}} = \underbrace{\lambda_f (\mathcal{L}_{\text{KL}}^{\text{fine}} + \gamma \mathcal{L}_{\text{MSE}}^{\text{fine}})}_{\text{Local Structure}} + \underbrace{\lambda_c \mathcal{L}_{\text{KL}}^{\text{coarse}}}_{\text{Global Dynamics}}. \quad (6)$$

The fine-grained components align code distributions and stabilize latent features, while the coarse objective captures high-level semantics:

$$\mathcal{L}_{\text{KL}}^{\text{fine}} = \sum_i D_{\text{KL}}(\mathbf{p}_{t+1,i}^{\text{fine}} \parallel \hat{\mathbf{p}}_{t+1,i}^{\text{fine}}), \quad (7)$$

$$\mathcal{L}_{\text{MSE}}^{\text{fine}} = \sum_i \|\mathbf{z}_{t+1,i} - \hat{\mathbf{z}}_{t+1,i}\|_2^2, \quad (8)$$

$$\mathcal{L}_{\text{KL}}^{\text{coarse}} = D_{\text{KL}}(\mathbf{p}_{t+1}^{\text{coarse}} \parallel \hat{\mathbf{p}}_{t+1}^{\text{coarse}}). \quad (9)$$

Here, D_{KL} denotes the Kullback–Leibler divergence. λ_f and λ_c balance patch-level supervision with window-level consistency. Since the targets \mathbf{p} are probability vectors produced by the softmax codebook (i.e., $\mathbf{p} \in \Delta^{K-1}$), KL provides a principled objective for distributional alignment in the code space, rather than treating codes as unconstrained Euclidean regressands. In addition, the momentum-updated EMA branch yields slowly varying targets, which stabilizes self-distillation and makes KL matching better conditioned during training.

(B) Codebook Objective ($\mathcal{L}_{\text{code}}$). A well-behaved bottleneck requires more than defining soft assignments: during training, the code space must stay synchronized with the encoder features, and the assignment distributions must avoid becoming either overly diffuse or collapsed to a few indices. Accordingly, we regularize the soft codebook with (i) prototype–feature alignment and (ii) dual-entropy calibration:

$$\mathcal{L}_{\text{code}} = \underbrace{\lambda_{\text{emb}} \mathcal{L}_{\text{emb}} + \lambda_{\text{com}} \mathcal{L}_{\text{com}}}_{\text{Codebook alignment}} + \underbrace{\lambda_{\text{ent}}^{\text{sample}} \mathcal{L}_{\text{ent}}^{\text{sample}} - \lambda_{\text{ent}}^{\text{batch}} \mathcal{L}_{\text{ent}}^{\text{batch}}}_{\text{Entropy}}. \quad (10)$$

The alignment terms couple continuous encoder features $\mathbf{h}_{t,i}$ with their soft-quantized embeddings $\mathbf{z}_{t,i}$ via a bidirectional objective:

$$\mathcal{L}_{\text{emb}} = \sum_i \|\text{sg}(\mathbf{z}_{t,i}) - \mathbf{h}_{t,i}\|_2^2, \quad (11)$$

$$\mathcal{L}_{\text{com}} = \sum_i \|\mathbf{z}_{t,i} - \text{sg}(\mathbf{h}_{t,i})\|_2^2, \quad (12)$$

where $\text{sg}(\cdot)$ denotes the stop-gradient operator.

Meanwhile, we calibrate the assignment distributions through dual-entropy control:

$$\mathcal{L}_{\text{ent}}^{\text{sample}} = \mathbb{E}[H(\mathbf{p})], \quad \mathcal{L}_{\text{ent}}^{\text{batch}} = H(\mathbb{E}[\mathbf{p}]). \quad (13)$$

In particular, minimizing $\mathcal{L}_{\text{ent}}^{\text{sample}}$ sharpens per-sample assignments and encourages decisive code selection, whereas maximizing $\mathcal{L}_{\text{ent}}^{\text{batch}}$ promotes diverse code usage across the

Table 1. Performance comparison on four benchmark datasets. All metrics are reported in percentage (%) and averaged over five independent runs. Best baselines are underlined.

Models	MSL				SMAP				SWaT				PSM			
	F1	AUC	Prec	Rec												
K-Means	20.63	52.17	19.27	31.34	8.74	39.82	10.52	10.16	14.45	62.20	7.99	<u>77.05</u>	42.75	51.37	30.40	78.89
DeepSVDD	23.46	53.67	14.78	73.87	22.05	44.07	12.90	<u>81.99</u>	15.28	58.22	12.65	20.00	44.45	49.95	30.31	89.38
LSTM-VAE	22.42	55.22	20.84	32.43	22.77	52.97	14.35	55.39	54.60	79.91	64.92	50.07	56.73	71.95	49.32	66.86
iTransformer	27.25	64.61	16.71	75.40	<u>33.00</u>	60.91	22.67	64.32	70.49	82.10	<u>98.17</u>	55.00	54.12	63.09	37.37	98.29
TimesNet	<u>28.44</u>	59.70	30.31	36.59	27.78	57.01	17.98	62.81	67.20	83.24	90.87	54.42	52.64	56.12	35.76	<u>99.71</u>
PAD	21.67	55.97	12.19	<u>97.78</u>	26.92	59.79	18.15	55.00	69.75	83.71	81.54	62.79	57.82	73.84	57.54	58.57
TS-JEPA	25.49	60.33	17.10	56.84	26.57	57.38	18.23	49.73	<u>71.95</u>	80.33	84.32	62.76	53.32	66.10	36.95	96.29
PatchTST	26.98	60.43	<u>75.00</u>	16.45	30.06	<u>61.62</u>	21.76	49.06	70.64	81.93	94.03	57.58	<u>58.17</u>	<u>75.76</u>	<u>64.68</u>	52.86
TS2Vec	23.48	64.86	31.45	18.82	32.81	61.48	<u>23.81</u>	52.81	67.00	<u>83.76</u>	80.95	57.17	48.43	72.13	32.39	95.96
MTS-JEPA	33.58	66.08	35.87	40.80	33.64	65.41	24.24	56.02	72.89	84.95	98.00	58.05	61.61	77.85	55.01	72.00

dataset, mitigating index collapse. Together, these terms keep the prototype set aligned with the evolving feature space while maintaining stable, informative code distributions for downstream prediction.

(C) Reconstruction Objective (\mathcal{L}_{rec}). To anchor latent representations and prevent collapse, we minimize the reconstruction error between the input patches and their reconstructions (after denormalization):

$$\mathcal{L}_{\text{rec}} = \sum_{i=1}^P \left\| \hat{\mathbf{X}}_{t,i} - \mathbf{X}_{t,i} \right\|_2^2. \quad (14)$$

Here $\hat{\mathbf{X}}_{t,i}$ is denormalized using the cached RevIN statistics of window t before computing \mathcal{L}_{rec} .

4. Experiments

4.1. Experimental Setup

Datasets. We evaluate on four widely-used multivariate anomaly detection benchmarks spanning spacecraft telemetry, industrial control, and cloud services. Mars Science Laboratory (MSL) and Soil Moisture Active Passive (SMAP) are NASA spacecraft telemetry datasets (Hundman et al., 2018). Secure Water Treatment (SWaT) is an industrial control system (ICS) water-treatment testbed with attack scenarios (Goh et al., 2017). Pooled Server Metrics (PSM) is a public server monitoring dataset collected from eBay production machines (Su et al., 2019). Detailed dataset statistics and preprocessing protocols are provided in Appendix B.1.

Training & Evaluation Protocol. We convert each multivariate stream into non-overlapping context-target pairs with stride 100, yielding windows with context length $T_c = 100$ and target length $T_t = 100$. Each window is tokenized into $P = 5$ non-overlapping patches of length

$L = 20$. We use a two-phase pipeline. In self-supervised pre-training, we train on the official training set without labels and use a 9:1 train-validation split for model selection and early stopping. For downstream training on the official test set, we adopt a 6:2:2 chronological split: we train the classifier on the training split, select the detection threshold on the validation split, and then fix it for final evaluation on the held-out test split. We report window-level Precision, Recall, F1, and AUC. Full implementation details, hyperparameters, and the downstream protocol are provided in Appendix B.2 and Appendix B.4.

4.2. Results

Baselines. To evaluate MTS-JEPA, we benchmark against nine diverse baselines. K-Means (MacQueen, 1967) and DeepSVDD (Ruff et al., 2018) represent classical clustering and deep one-class classification. LSTM-VAE (Park et al., 2018) serves as a standard RNN-based reconstruction baseline. TS2Vec (Yue et al., 2022) is included as a state-of-the-art contrastive learner. We also compare against advanced backbones, including TimesNet (Wu et al., 2023) for 2D temporal variations, PatchTST (Nie et al., 2023) as a patch-based Transformer, and iTransformer (Liu et al., 2024) for variate-wise attention. We additionally include PAD (Jhin et al., 2023), a recent anomaly prediction model for direct comparison. Finally, we include TS-JEPA (Ennadir et al., 2025) to directly assess the improvements of our multi-resolution design over a standard single-scale JEPA baseline. When applicable, baselines are pre-trained on the same data and aligned to the anomaly prediction setting. Specifically, detection methods evaluate normality directly on the observation window \mathbf{X}_t , while forecasting models utilize prediction errors on the target data, and representation learners (e.g., TS2Vec) use the same classifier head on the embeddings.

Main results. Table 1 reports the mean anomaly prediction results on four benchmarks using the same data splits and five random seeds. Full results are available in Appendix C. Under this setting, MTS-JEPA achieves the top AUC on all datasets, suggesting consistently strong ranking quality for upcoming abnormal windows under our precursor-based definition. Moreover, MTS-JEPA attains best F1 performance across benchmarks, indicating that its ranking quality can translate into effective decisions under the shared threshold-selection procedure.

The trends of competing baselines are broadly consistent with their modeling assumptions. Classical methods such as K-Means and DeepSVDD rely on static similarity or compactness in a feature space, which can be less sensitive when precursor windows deviate only mildly from normal patterns. Reconstruction-based models such as LSTM-VAE may also be less aligned with a precursor setting, since reconstruction error often becomes more distinctive after abnormal behavior has developed. In addition, a set of advanced time-series backbones, including TimesNet, TS2Vec, PatchTST, and iTransformer, provide strong sequence representations and capture long-range dependencies. In our anomaly prediction setting, however, these general-purpose backbones are not directly optimized for highlighting weak early-stage transitions toward future abnormalities, so their scores can be less separable when the precursor signal is subtle and noisy. Likewise, the inferior performance of TS-JEPA highlights the limitations of a pure continuous predictive model; lacking both a discrete codebook and multi-resolution modeling, it suffers from optimization instability and fails to capture diverse precursor dynamics. Finally, while PAD is explicitly designed for anomaly prediction, it relies on a single-scale objective that restricts its ability to decouple complex latent evolution from stochastic noise.

4.3. Generality

A practical time-series model should remain effective under distribution shifts, where the pre-training data may differ substantially from the deployment environment. To assess such transferability, Table 2 reports generality results under two pre-training settings. In-domain pre-training uses the official training set of the target dataset, while cross-domain pre-training uses the union of the other three datasets, with the target dataset fully excluded during pre-training. In both cases, we keep the downstream evaluation protocol identical on the target dataset, so the only difference comes from the source of pre-training data. We select TS2Vec and PatchTST for this generality study since they perform strongly in our main table under our setting, and thus provide meaningful SOTA references for evaluating transferability.

With this setup, Table 2 shows that cross-domain transfer is

Table 2. In-domain and cross-domain generalization comparison. We report mean F1-score and AUC (%) averaged over 5 runs with different random seeds. ID: in-domain; CD: cross-domain; Abs. Diff. = CD-ID; Rel. Diff. = (CD-ID)/ID (%).

Models	Settings	MSL		SMAP		SWaT		PSM	
		F1	AUC	F1	AUC	F1	AUC	F1	AUC
PatchTST	ID	26.98	60.43	30.06	61.62	70.64	81.93	58.17	75.76
	CD	27.08	60.80	26.21	58.77	54.34	68.76	50.07	53.72
	Abs. Diff.	+0.10	+0.37	-3.85	-2.85	-16.30	-13.17	-8.10	-22.04
	Rel. Diff.	+0.37%	+0.61%	-12.81%	-4.63%	-23.07%	-16.07%	-13.92%	-29.09%
TS2Vec	ID	23.48	64.86	32.81	61.48	67.00	83.76	48.43	72.13
	CD	22.87	62.00	26.99	57.54	65.08	82.91	48.15	56.22
	Abs. Diff.	-0.61	-2.86	-5.82	-3.94	-1.92	-0.85	-0.28	-15.91
	Rel. Diff.	-2.60%	-4.41%	-17.74%	-6.41%	-2.87%	-1.01%	-0.58%	-22.06%
MTS-JEPA	ID	33.58	66.08	33.64	65.41	72.89	84.95	61.61	77.85
	CD	33.48	67.13	33.81	68.88	71.10	82.96	56.87	66.80
	Abs. Diff.	-0.10	+1.05	+0.17	+3.47	-1.79	-1.99	-4.74	-11.05
	Rel. Diff.	-0.30%	+1.59%	+0.51%	+5.30%	-2.46%	-2.34%	-7.69%	-14.19%

Table 3. Ablation results demonstrating the contribution of each model component on four benchmark datasets. All metrics are reported in percentages.

Model Variant	MSL		SMAP		SWaT		PSM	
Metric	F1	AUC	F1	AUC	F1	AUC	F1	AUC
w/o KL	29.01	53.90	28.71	60.19	67.33	79.95	54.93	70.83
w/o Reconstruction	25.96	52.68	25.15	52.80	14.77	53.30	53.03	69.84
w/o Predictive Objective	28.88	53.17	27.05	59.81	59.47	78.60	58.89	70.17
w/o Codebook Loss	31.62	58.93	31.53	62.06	72.64	82.63	60.83	75.85
w/o Codebook Module	21.82	43.02	21.69	51.00	11.51	50.00	53.03	46.61
w/o Downsample	28.77	63.16	30.39	61.34	71.62	83.60	60.79	71.72
Full Model	33.58	66.08	33.64	65.41	72.89	84.95	61.61	77.85

generally more challenging, and performance can decrease when the pre-training data comes from different datasets, which is consistent with the presence of domain shift. Notably, MTS-JEPA continues to perform competitively across benchmarks. We observe that its AUC remains comparable to the in-domain setting on several datasets and can improve modestly in some cases, suggesting that the learned scores preserve useful ranking information even when the target dataset is excluded during pre-training. On more challenging data such as PSM, all methods experience a clear drop, yet MTS-JEPA retains relatively strong performance compared to the evaluated backbones. Overall, these results provide additional evidence that the model transfers reasonably well across datasets, particularly when assessed through threshold-free ranking metrics.

4.4. Model Analysis

4.4.1. ABLATION STUDY

Since MTS-JEPA integrates multiple mechanisms, it is important to attribute the observed gains to the intended design choices rather than a single component. We therefore conduct a systematic ablation study by selectively removing modules, as summarized in Table 3. We observe that the predictive objective is the primary engine for capturing temporal dependencies; removing it causes a significant drop, and the KL term proves superior to MSE alone by

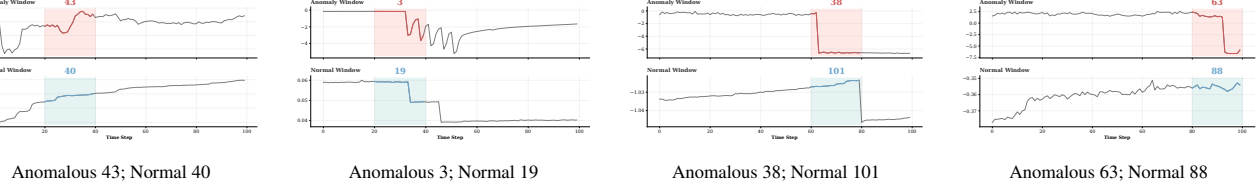


Figure 3. Window-level comparisons of dominant latent codes between anomalous and normal windows on the PSM dataset. Shaded regions indicate patch-level segments where the dominant code is selected.

enforcing precise distributional alignment. Furthermore, the results validate that multi-resolution modeling is essential for outperforming baselines, as it enables the capture of coarse-grained precursors that single-scale models miss. Conversely, reconstruction serves as a non-negotiable anchor; its removal triggers model collapse, confirming its role in preventing latent degeneration.

Among all variants, the most consequential one is removing the soft codebook bottleneck (w/o Codebook Module): performance collapses to near-random, while removing only the auxiliary regularizers yields a much smaller drop. It suggests that beyond providing discrete, prototype-anchored regime codes, the bottleneck may also play a critical role in optimization stability. This naturally raises a question: what stabilizing effect does the bottleneck introduce that the auxiliary losses alone do not?

The ablations offer an empirical explanation consistent with our formulation. With the codebook in place, self-distillation operates as KL matching between probability codes on the simplex (Eq. 3), so the predictor tracks a bounded distributional trajectory instead of performing unconstrained regression in \mathbb{R}^D . In conjunction with slowly varying EMA targets, this bounded code space appears to provide a more stable reference for self-distillation (Zhou et al., 2022). Once we remove the bottleneck, this constrained code space disappears, so KL alignment loses its natural domain, and training degenerates into an ill-conditioned matching problem, consistent with the observed near-collapse. By contrast, removing only the auxiliary codebook losses causes only a mild drop for w/o Codebook Loss. These auxiliary losses mainly serve as an outperformance mechanism that further boosts an already strong model.

4.4.2. VISUALIZATION OF LEARNED REGIMES

In the Introduction, we hypothesized that a discrete bottleneck would sharpen the distinction between normal dynamics and structural anomalies. Furthermore, in Section 3.3, we designed the codebook Q specifically to capture regime-like patterns via finite prototypes $\{c_k\}$. Here, we empirically verify whether the learned representations align with these methodological motivations.

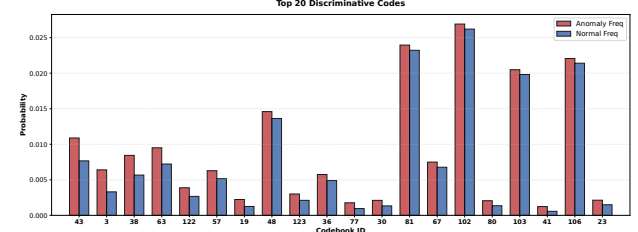


Figure 4. Histogram comparing the occurrence probability of latent codes in anomalous versus normal windows on the PSM test set. The codes are sorted by their anomaly–normal probability difference (from largest to smallest). PSM is used because it provides a large test set with reliable window-level anomaly labels.

First, we examine the activation statistics of the codebook. Figure 4 reports a quantitative study on the PSM dataset, ranking codes by the absolute frequency gap between normal and anomalous windows. We observe that a small subset of codes exhibits pronounced activation gaps, suggesting that the model naturally learns to partition the latent space into condition-dependent regions without explicit supervision.

To further validate this structure qualitatively, Figure 3 maps the most discriminative codes back to their original time-series patches. We observe that, within the same temporal context, distinct codes consistently correspond to distinct physical behaviors. This alignment confirms that the discrete formulation effectively disentangles diverse local dynamics into a finite set of identifiable regimes. Consequently, the codebook successfully distinguishes precursor-like patterns from normal dynamics, providing a discriminative structural basis for anomaly prediction even under distribution shift.

5. Conclusion

This work introduces MTS-JEPA, advancing anomaly prediction from reactive detection to proactive world modeling. By synergizing multi-resolution views with a soft-quantized bottleneck, our architecture effectively captures scale-variant precursors while mitigating the representation collapse often observed in continuous self-supervision. Our empirical and theoretical analysis reveals that the discrete

bottleneck serves as a critical regularizer, enabling stable optimization without explicit negative sampling. Extensive experiments confirm that MTS-JEPA achieves state-of-the-art performance in early-warning scenarios, suggesting that discrete latent dynamics offer a robust foundation for future research in reliable autonomous systems.

Impact Statement

This work advances the reliability and safety of critical infrastructure by enabling proactive anomaly prediction in complex multivariate systems, such as industrial control and server operations. By shifting from reactive detection to early warning, MTS-JEPA has the potential to mitigate catastrophic failures, reduce operational downtime, and improve resource efficiency in automated environments. While the proposed method is general-purpose, its primary societal impact lies in enhancing the resilience of essential services and high-stakes machinery.

References

Assran, M., Duval, Q., Misra, I., Bojanowski, P., Vincent, P., Rabbat, M., LeCun, Y., and Ballas, N. Self-supervised learning from images with a Joint-Embedding predictive architecture. In *Proceedings of the IEEE/CVF Conference on Computer Vision and Pattern Recognition*, pp. 15619–15629, 2023.

Bardes, A., Garrido, Q., Ponce, J., Chen, X., Rabbat, M., LeCun, Y., Assran, M., and Ballas, N. Revisiting feature prediction for learning visual representations from video. *Transactions on Machine Learning Research*, 2024. ISSN 2835-8856.

Chen, X. and He, K. Exploring simple siamese representation learning. In *Proceedings of the IEEE/CVF Conference on Computer Vision and Pattern Recognition*, pp. 15750–15758, 2021.

Cover, T. M. and Thomas, J. A. *Elements of Information Theory*. Wiley-Interscience, Hoboken, N.J., 2nd edition, 2006.

Ennadir, S., Golkar, S., and Sarra, L. Joint embeddings go temporal. *arXiv preprint arXiv:2509.25449*, 2025.

Goh, J., Adepu, S., Junejo, K. N., and Mathur, A. A dataset to support research in the design of secure water treatment systems. In Havarneanu, G., Setola, R., Nassopoulos, H., and Wolthusen, S. (eds.), *Critical Information Infrastructures Security*, pp. 88–99, Cham, 2017. Springer International Publishing.

Gong, D., Liu, L., Le, V., Saha, B., Mansour, M. R., Venkatesh, S., and Hengel, A. v. d. Memorizing normality to detect anomaly: Memory-augmented deep autoencoder for unsupervised anomaly detection. In *Proceedings of the IEEE/CVF International Conference on Computer Vision*, pp. 1705–1714, 2019.

Hundman, K., Constantinou, V., Laporte, C., Colwell, I., and Soderstrom, T. Detecting spacecraft anomalies using LSTMs and nonparametric dynamic thresholding. In *Proceedings of the 24th ACM SIGKDD International Conference on Knowledge Discovery and Data Mining*, pp. 387–395, 2018.

Jhin, S. Y., Lee, J., and Park, N. Precursor-of-anomaly detection for irregular time series. In *Proceedings of the 29th ACM SIGKDD International Conference on Knowledge Discovery and Data Mining*, pp. 917–929, 2023.

Kim, T., Kim, J., Tae, Y., Park, C., Choi, J.-H., and Choo, J. Reversible instance normalization for accurate time-series forecasting against distribution shift. In *International Conference on Learning Representations*, 2022.

Lee, D., Malacarne, S., and Aune, E. Vector quantized time series generation with a bidirectional prior model. In *Proceedings of the 26th International Conference on Artificial Intelligence and Statistics*, 2023.

Lee, D., Malacarne, S., and Aune, E. Explainable time series anomaly detection using masked latent generative modeling. *Pattern Recognition*, 156:110826, 2024.

Lin, T.-Y., Dollár, P., Girshick, R., He, K., Hariharan, B., and Belongie, S. Feature pyramid networks for object detection. In *Proceedings of the IEEE/CVF Conference on Computer Vision and Pattern Recognition*, pp. 2117–2125, 2017.

Liu, M., Zeng, A., Chen, M., Xu, Z., Lai, Q., Ma, L., and Xu, Q. SCINet: Time series modeling and forecasting with sample convolution and interaction. *Advances in Neural Information Processing Systems*, 35:5816–5828, 2022a.

Liu, S., Yu, H., Liao, C., Li, J., Lin, W., Liu, A. X., and Dustdar, S. Pyraformer: Low-complexity pyramidal attention for long-range time series modeling and forecasting. In *International Conference on Learning Representations*, 2022b.

Liu, Y., Hu, T., Zhang, H., Wu, H., Wang, S., Ma, L., and Long, M. iTransformer: Inverted transformers are effective for time series forecasting. In *International Conference on Learning Representations*, 2024.

MacQueen, J. Some methods for classification and analysis of multivariate observations. In *Proceedings of the 5th Berkeley Symposium on Mathematical Statistics and Probability, Volume 1*, pp. 281–297. University of California Press, 1967.

Nie, Y., Nguyen, N. H., Sinthong, P., and Kalagnanam, J. A time series is worth 64 words: Long-term forecasting with transformers. In *International Conference on Learning Representations*, 2023.

Park, D., Hoshi, Y., and Kemp, C. C. A multimodal anomaly detector for robot-assisted feeding using an LSTM-based variational autoencoder. *IEEE Robotics and Automation Letters*, 3(3):1544–1551, 2018.

Park, M.-Y., Lee, W.-J., Kim, S. T., and Park, G.-M. When will it fail?: Anomaly to prompt for forecasting future anomalies in time series. *arXiv preprint arXiv:2506.23596*, 2025.

Ruff, L., Vandermeulen, R., Goernitz, N., Deecke, L., Siddiqui, S. A., Binder, A., Müller, E., and Kloft, M. Deep one-class classification. In *International Conference on Machine Learning*, pp. 4393–4402, 2018.

Su, Y., Zhao, Y., Niu, C., Liu, R., Sun, W., and Pei, D. Robust anomaly detection for multivariate time series through stochastic recurrent neural networks. In *Proceedings of the 25th ACM SIGKDD International Conference on Knowledge Discovery and Data Mining*, 2019.

Tian, Y., Chen, X., and Ganguli, S. Understanding self-supervised learning dynamics without contrastive pairs. In *International Conference on Machine Learning*, pp. 10268–10278. PMLR, 2021.

Van Den Oord, A., Vinyals, O., et al. Neural discrete representation learning. *Advances in Neural Information Processing Systems*, 30, 2017.

Wang, S., Wu, H., Shi, X., Hu, T., Luo, H., Ma, L., Zhang, J. Y., and Zhou, J. TimeMixer: Decomposable multi-scale mixing for time series forecasting. In *International Conference on Learning Representations*, 2024.

Wen, Y., Ma, T., Weng, L., Nguyen, L., and Julius, A. A. Abstracted shapes as tokens-a generalizable and interpretable model for time-series classification. *Advances in Neural Information Processing Systems*, 37:92246–92272, 2025.

Wu, H., Hu, T., Liu, Y., Zhou, H., Wang, J., and Long, M. TimesNet: Temporal 2d-variation modeling for general time series analysis. In *International Conference on Learning Representations*, 2023.

Xu, J., Wu, H., Wang, J., and Long, M. Anomaly transformer: Time series anomaly detection with association discrepancy. In *International Conference on Learning Representations*, 2022.

Yue, Z., Wang, Y., Duan, J., Yang, T., Huang, C., Tong, Y., and Xu, B. TS2Vec: Towards universal representation of time series. In *Proceedings of the AAAI Conference on Artificial Intelligence*, volume 36, pp. 8980–8987, 2022.

Zhao, S., Wang, W., Xu, H., Yu, Z., Wen, Q., Wang, G., and Pang, G. Abnormality forecasting: Time series anomaly prediction via future context modeling. *arXiv preprint arXiv:2410.12206*, 2024.

Zhou, H., Zhang, S., Peng, J., Zhang, S., Li, J., Xiong, H., and Zhang, W. Informer: Beyond efficient transformer for long sequence time-series forecasting. In *Proceedings of the AAAI Conference on Artificial Intelligence*, volume 35, pp. 11106–11115, 2021.

Zhou, J., Wei, C., Wang, H., Shen, W., Xie, C., Yuille, A., and Kong, T. Image BERT pre-training with online tokenizer. In *International Conference on Learning Representations*, 2022.

A. Methodological Details

A.1. Notations

Table 4. Categorized notations.

Category	Symbol	Description	Category	Symbol	Description
Dimensions	T, V	Time series size ($T \times V$)	Data Inputs	\mathbf{x}	Input time series
	T_w	Window length		$\hat{\mathbf{W}}_t$	Normalized window
	N	Number of windows		$\mathbf{X}_t^{\text{fine}}$	Fine view (patches)
	P	Num. patches ($T_w = P \cdot L$)		$\mathbf{X}_t^{\text{coarse}}$	Coarse view (downsampled)
	L	Patch length	Representations	\mathbf{h}_t	Encoder latent rep.
	K	Codebook size		\mathbf{c}_k	Learnable prototype
	D	Embedding dimension		$\mathbf{p}_{t,i}$	Code-assignment prob.
Hyperparams	τ	Soft-max temperature		Π_t	Code sequence
	λ_{\dots}	Loss balancing weights		$\mathbf{z}_{t,i}$	Soft-quantized embedding
	γ	MSE local weight		\mathbf{q}	Coarse query token
Architecture	\mathcal{E}_θ	Online encoder	Outputs	$\hat{\Pi}^{\text{fine}}$	Predicted fine code dist.
	\mathcal{E}_ξ	EMA encoder		$\hat{\Pi}^{\text{coarse}}$	Predicted coarse code dist.
	\mathcal{Q}	Codebook bottleneck		$\hat{\mathbf{z}}_{t,i}$	Predicted embedding
	\mathcal{D}	Reconstruction decoder		$\hat{\mathbf{X}}_{t,i}$	Reconstructed patch
	sg	Stop-gradient operator	Objectives	$\mathcal{L}_{\text{pred/code}}$	Predictive / Code losses
				$\mathcal{L}_{\text{rec/total}}$	Recon. / Total losses

A.2. Time-Axis Downsampling

DownAvg operator. Given a normalized window $\hat{\mathbf{W}}_t \in \mathbb{R}^{T_w \times V}$ with $T_w = P \cdot L$, we define $\text{DownAvg}_P(\cdot)$ as a time-axis downsampling operator that averages every P consecutive time points (stride P) for each variable:

$$\mathbf{X}_t^{\text{coarse}} = \text{DownAvg}_P(\hat{\mathbf{W}}_t) \in \mathbb{R}^{1 \times L \times V}. \quad (15)$$

Equivalently, for within-patch index $\ell \in [L]$ and variable $v \in [V]$:

$$[\mathbf{X}_t^{\text{coarse}}]_{1,\ell,v} = \frac{1}{P} \sum_{j=1}^P \hat{\mathbf{W}}_t[(\ell-1)P+j, v]. \quad (16)$$

A.3. Theoretical Analysis of Latent Stability

In this subsection, we provide the formal proofs for the stability properties of the MTS-JEPA latent space. We demonstrate how the soft codebook acts as a geometric constraint that explicitly bounds representation drift. We provide two complementary guarantees: (i) an upper bound on representation drift (stability), and (ii) a lower bound that rules out the trivial constant solution (non-collapse).

A.3.1. STABILITY UPPER BOUND

This part proves an explicit upper bound on representation drift in embedding space. The argument follows a short chain: we first fix a bounded latent geometry via the soft codebook, then establish a probability-to-geometry bridge ($\ell_1 \rightarrow \ell_2$), and finally combine this bridge with EMA smoothness and predictive alignment to obtain Theorem A.3.

Preliminaries. Continuous forecasting models can exhibit collapse or explosion, making the latent geometry unstable. The soft codebook eliminates this degree of freedom by restricting every soft-quantized embedding to the convex hull of a

finite prototype set. In particular, the radius constant M defined below will be the only scale factor that propagates into the final drift bound.

Definition A.1 (Soft Code Map). Let $K \geq 2$ be the number of discrete prototypes and $D \geq 1$ be the embedding dimension. Let $\mathbf{C} \in \mathbb{R}^{K \times D}$ be the codebook matrix where the k -th **row** corresponds to the prototype \mathbf{c}_k . We define the probability simplex $\Delta^{K-1} := \{\mathbf{p} \in \mathbb{R}^K : \mathbf{p} \succeq \mathbf{0}, \mathbf{1}^\top \mathbf{p} = 1\}$.

The **soft-quantization map** $z : \Delta^{K-1} \rightarrow \mathbb{R}^D$ is defined as the expected embedding:

$$z(\mathbf{p}) := \mathbf{C}^\top \mathbf{p} = \sum_{k=1}^K p_k \mathbf{c}_k. \quad (17)$$

We further define the **geometric radius** M as the maximum Euclidean norm of any prototype...

Lipschitz Bound. Training is performed in probability space (via KL divergence), whereas drift and anomaly scores are measured in embedding space. We therefore need a simple link that converts discrepancies between assignment distributions into Euclidean changes after soft quantization. Lemma A.2 provides exactly this bridge, with the codebook radius M as the controlling constant.

Lemma A.2 ($\ell_1 \rightarrow \ell_2$ Lipschitzness). *For any two assignment distributions $\mathbf{p}, \mathbf{q} \in \Delta^{K-1}$, the Euclidean distance between their soft-quantized embeddings is bounded by their ℓ_1 distance, scaled by the codebook radius M :*

$$\|z(\mathbf{p}) - z(\mathbf{q})\|_2 \leq M \|\mathbf{p} - \mathbf{q}\|_1. \quad (18)$$

Proof. We expand the Euclidean distance and apply the triangle inequality.

$$\begin{aligned} \|z(\mathbf{p}) - z(\mathbf{q})\|_2 &= \left\| \sum_{k=1}^K p_k \mathbf{c}_k - \sum_{k=1}^K q_k \mathbf{c}_k \right\|_2 \\ &= \left\| \sum_{k=1}^K (p_k - q_k) \mathbf{c}_k \right\|_2 \\ &\leq \sum_{k=1}^K |p_k - q_k| \cdot \|\mathbf{c}_k\|_2. \end{aligned}$$

Since $\|\mathbf{c}_k\|_2 \leq M$ for all k , we have:

$$\sum_{k=1}^K |p_k - q_k| \cdot \|\mathbf{c}_k\|_2 \leq M \sum_{k=1}^K |p_k - q_k| = M \|\mathbf{p} - \mathbf{q}\|_1.$$

□

With this bridge in place, the remaining step is to control the probability-space differences themselves. Predictive alignment bounds the deviation between targets and predictions at each time step, while EMA smoothness bounds how fast the target moves. Combining these two controls yields the following stability bound.

Theorem A.3 (Stability Bound). *Let $\{\hat{\mathbf{p}}_t\}$ and $\{\mathbf{p}_t\}$ be the sequences of predicted and target (EMA) distributions, respectively, and let $\hat{\mathbf{z}}_t = z(\hat{\mathbf{p}}_t)$. Assume the following conditions hold for time steps t and $t+1$:*

1. **Predictive Alignment:** $D_{\text{KL}}(\mathbf{p}_t \|\hat{\mathbf{p}}_t) \leq \varepsilon_t$ and $D_{\text{KL}}(\mathbf{p}_{t+1} \|\hat{\mathbf{p}}_{t+1}) \leq \varepsilon_{t+1}$.
2. **Target Smoothness:** $\|\mathbf{p}_{t+1} - \mathbf{p}_t\|_1 \leq \delta_t$.

Then, the representation drift $\|\hat{\mathbf{z}}_{t+1} - \hat{\mathbf{z}}_t\|_2$ is bounded by:

$$\|\hat{\mathbf{z}}_{t+1} - \hat{\mathbf{z}}_t\|_2 \leq M \left(\sqrt{2\varepsilon_{t+1}} + \delta_t + \sqrt{2\varepsilon_t} \right). \quad (19)$$

Proof. First, we recall **Pinsker's Inequality** (Cover & Thomas, 2006), which provides a bound on the ℓ_1 distance between two distributions in terms of their KL divergence:

$$\|\mathbf{p} - \mathbf{q}\|_1 \leq \sqrt{2D_{\text{KL}}(\mathbf{p}\|\mathbf{q})}.$$

We now decompose the drift term $\|\hat{\mathbf{z}}_{t+1} - \hat{\mathbf{z}}_t\|_2$ using the triangle inequality by introducing the intermediate target embeddings \mathbf{z}_{t+1} and \mathbf{z}_t :

$$\begin{aligned} \|\hat{\mathbf{z}}_{t+1} - \hat{\mathbf{z}}_t\|_2 &= \|\hat{\mathbf{z}}_{t+1} - \mathbf{z}_{t+1} + \mathbf{z}_{t+1} - \mathbf{z}_t + \mathbf{z}_t - \hat{\mathbf{z}}_t\|_2 \\ &\leq \underbrace{\|\hat{\mathbf{z}}_{t+1} - \mathbf{z}_{t+1}\|_2}_{(A)} + \underbrace{\|\mathbf{z}_{t+1} - \mathbf{z}_t\|_2}_{(B)} + \underbrace{\|\mathbf{z}_t - \hat{\mathbf{z}}_t\|_2}_{(C)}. \end{aligned}$$

Bounding (A) and (C): Using Lemma A.2 and Pinsker's Inequality:

$$\|\hat{\mathbf{z}}_{t+1} - \mathbf{z}_{t+1}\|_2 \leq M\|\hat{\mathbf{p}}_{t+1} - \mathbf{p}_{t+1}\|_1 \leq M\sqrt{2\varepsilon_{t+1}}.$$

By symmetry, $\|\mathbf{z}_t - \hat{\mathbf{z}}_t\|_2 \leq M\sqrt{2\varepsilon_t}$.

Bounding (B): Using Lemma A.2 and the smoothness assumption:

$$\|\mathbf{z}_{t+1} - \mathbf{z}_t\|_2 \leq M\|\mathbf{p}_{t+1} - \mathbf{p}_t\|_1 \leq M\delta_t.$$

Summing these terms yields the final bound. \square

Interpretation. This theorem implies that the sensitivity of our anomaly score is strictly controlled by the codebook radius M . Unlike unconstrained continuous models where gradients can cause unbounded output shifts (effectively $M \rightarrow \infty$), MTS-JEPA guarantees that any significant representation drift arises from either a true shift in the target signal (δ_t) or a high prediction error (ε). This effectively filters out false positives caused by trivial numerical perturbations.

A.3.2. NON-COLLAPSE LOWER BOUND

Goal. We provide a simple *non-collapse certificate* for the soft codebook. Namely, if a mini-batch exhibits (i) non-trivial multi-code usage, (ii) sufficiently sharp assignments, and (iii) non-negligible separation between two frequently used prototypes, then the soft-quantized embeddings $\mathbf{z}_i = \mathbf{C}^\top \mathbf{p}_i$ have strictly positive batch variance, i.e., $\text{Tr}(\text{Cov}(\{\mathbf{z}_i\})) > 0$.

Setup. Consider a batch of assignment probabilities $\{\mathbf{p}_i\}_{i=1}^B \subset \Delta^{K-1}$ and their average $\bar{\mathbf{p}} := \frac{1}{B} \sum_{i=1}^B \mathbf{p}_i$. Let $\mathbf{z}_i := \mathbf{C}^\top \mathbf{p}_i \in \mathbb{R}^D$, where $\mathbf{C} \in \mathbb{R}^{K \times D}$ stacks prototypes as rows.

To preclude the constant-code corner case, we assume three mild properties. Crucially, these are not arbitrary assumptions but are explicitly enforced by the optimization objectives defined in Section 3.4:

- **Batch Entropy:** $\mathcal{L}_{\text{ent}}^{\text{batch}}$ maximizes $H(\bar{\mathbf{p}})$, enforcing Assumption A.4.
- **Sharpness:** $\mathcal{L}_{\text{ent}}^{\text{sample}}$ minimizes individual entropy, driving \mathbf{p}_i toward one-hot vectors (Assumption A.5).
- **Separation:** \mathcal{L}_{com} and EMA updates prevent prototype collapse (Assumption A.7).

Assumption A.4 (Multi-code usage / non-trivial batch marginal). The batch marginal $\bar{\mathbf{p}}$ is not concentrated on a single index. Concretely,

$$H(\bar{\mathbf{p}}) \geq \eta \quad \text{for some } \eta > 0. \quad (20)$$

Assumption A.5 (Assignment sharpness). For each sample, let $k(i) = \arg \max_k p_{i,k}$. There exists $\varepsilon \in [0, 1)$ such that

$$\|\mathbf{p}_i - \mathbf{e}_{k(i)}\|_1 \leq \varepsilon \quad \text{for all } i. \quad (21)$$

Remark A.6. The deviation ε is strictly controlled by the softmax temperature τ . As $\tau \rightarrow 0$, \mathbf{p}_i approaches a hard assignment, ensuring $\varepsilon \rightarrow 0$.

Assumption A.7 (Separation for the two dominant codes). Define

$$\beta := \frac{1 - \rho^*}{K - 1}, \quad (22)$$

where $\rho^* \in (1/K, 1)$ is the unique root of the equation $\mathcal{H}_b(\rho) + (1 - \rho) \log(K - 1) = \eta$. Let $m = \arg \max_k \bar{p}_k$ and let $r \neq m$ be any index satisfying $\bar{p}_r \geq \beta$ (guaranteed by Lemma A.8). Assume their prototypes satisfy

$$\|\mathbf{c}_m - \mathbf{c}_r\|_2 \geq \Delta_c \quad \text{for some } \Delta_c > 0. \quad (23)$$

To drive a variance lower bound, we first (Lemma A.8) extract two non-negligible codes from entropy, then (Lemma A.9) convert their marginal mass into two dominant-code groups under sharp assignments.

Lemma A.8 (Entropy lower bound implies at least two active codes). *Let $m = \arg \max_k \bar{p}_k$ and $\bar{p}_{\max} = \bar{p}_m$. If $H(\bar{\mathbf{p}}) \geq \eta$, then $\bar{p}_{\max} \leq \rho^*$, where ρ^* is defined in Assumption A.7. Moreover, there exists an index $r \neq m$ such that*

$$\bar{p}_r \geq \beta := \frac{1 - \rho^*}{K - 1}. \quad (24)$$

Proof. Consider the function $\phi(x) := \mathcal{H}_b(x) + (1 - x) \log(K - 1)$, which represents the maximum entropy achievable by a distribution with maximum probability mass x . It is well-known (from Fano's inequality analysis) that $\phi(x)$ is strictly decreasing for $x \in [1/K, 1]$. Since $H(\bar{\mathbf{p}}) \geq \eta$ and $H(\bar{\mathbf{p}}) \leq \phi(\bar{p}_{\max})$, we have $\phi(\bar{p}_{\max}) \geq \eta = \phi(\rho^*)$. By the monotonicity of ϕ , this implies $\bar{p}_{\max} \leq \rho^*$. Consequently, the remaining mass is at least $1 - \rho^*$. By the pigeonhole principle, at least one non-dominant index r must satisfy $\bar{p}_r \geq (1 - \rho^*)/(K - 1) = \beta$. \square

Lemma A.9 (Marginal mass transfers to dominant-code frequency). *Define $\hat{\pi}_k := \frac{1}{B} \sum_{i=1}^B \mathbb{I}[k(i) = k]$. Under Assumption A.5, we have $\|\bar{\mathbf{p}} - \hat{\mathbf{\pi}}\|_1 \leq \varepsilon$, hence for all k ,*

$$\hat{\pi}_k \geq \bar{p}_k - \varepsilon. \quad (25)$$

Proof.

$$\|\bar{\mathbf{p}} - \hat{\mathbf{\pi}}\|_1 = \left\| \frac{1}{B} \sum_{i=1}^B (\mathbf{p}_i - \mathbf{e}_{k(i)}) \right\|_1 \leq \frac{1}{B} \sum_{i=1}^B \|\mathbf{p}_i - \mathbf{e}_{k(i)}\|_1 \leq \varepsilon.$$

The coordinate-wise bound follows from $|\bar{p}_k - \hat{\pi}_k| \leq \|\bar{\mathbf{p}} - \hat{\mathbf{\pi}}\|_1$. \square

We will use the following prototype-proximity bound implied by sharp assignments: for any i ,

$$\|\mathbf{z}_i - \mathbf{c}_{k(i)}\|_2 \leq \left(\max_k \|\mathbf{c}_k\|_2 \right) \|\mathbf{p}_i - \mathbf{e}_{k(i)}\|_1 \leq M\varepsilon, \quad (26)$$

where $M := \max_k \|\mathbf{c}_k\|_2$.

Theorem A.10 (Explicit variance lower bound / non-collapse). *Under Assumptions A.4–A.7, let β be defined as in Assumption A.7 (i.e., $\beta = \frac{1 - \rho^*}{K - 1}$), and define*

$$\alpha := \max\{\beta - \varepsilon, 0\}.$$

Let (m, r) be the indices specified in Assumption A.7. If $\alpha > 0$ and $2M\varepsilon < \Delta_c$, then the batch covariance of $\{\mathbf{z}_i\}_{i=1}^B$ obeys

$$\text{Tr}(\text{Cov}(\{\mathbf{z}_i\})) \geq \alpha^2 (\Delta_c - 2M\varepsilon)^2 > 0. \quad (27)$$

Proof. Step 1 (two codes have non-trivial dominant frequency). Let $A = \{i : k(i) = m\}$ and $R = \{i : k(i) = r\}$. By Lemma A.8, $\bar{p}_r \geq \beta$. Since $m = \arg \max_k \bar{p}_k$, we also have $\bar{p}_m \geq \bar{p}_r \geq \beta$. Applying Lemma A.9 yields:

$$\Pr(i \in A) = \hat{\pi}_m \geq \bar{p}_m - \varepsilon \geq \beta - \varepsilon = \alpha,$$

$$\Pr(i \in R) = \hat{\pi}_r \geq \bar{p}_r - \varepsilon \geq \beta - \varepsilon = \alpha.$$

Step 2 (dominant-code membership implies proximity to the corresponding prototype). By (26) and Assumption A.5, we have tight concentration around prototypes:

$$i \in A \implies \|\mathbf{z}_i - \mathbf{c}_m\|_2 \leq M\varepsilon, \quad j \in R \implies \|\mathbf{z}_j - \mathbf{c}_r\|_2 \leq M\varepsilon.$$

Step 3 (two separated prototype-centered clusters imply positive covariance trace). For any $i \in A$ and $j \in R$, the triangle inequality gives:

$$\begin{aligned} \|\mathbf{z}_i - \mathbf{z}_j\|_2 &\geq \|\mathbf{c}_m - \mathbf{c}_r\|_2 - \|\mathbf{z}_i - \mathbf{c}_m\|_2 - \|\mathbf{z}_j - \mathbf{c}_r\|_2 \\ &\geq \Delta_c - 2M\varepsilon. \end{aligned}$$

Now view \mathbf{Z} as a random variable obtained by uniformly sampling an index from the batch, and let \mathbf{Z}' be an independent copy. The pairwise-variance identity yields $\text{Tr}(\text{Cov}(\mathbf{Z})) = \frac{1}{2} \mathbb{E}[\|\mathbf{Z} - \mathbf{Z}'\|_2^2]$. Restricting the expectation to the event $\{i \in A, j \in R\}$ yields the bound:

$$\begin{aligned} \text{Tr}(\text{Cov}(\mathbf{Z})) &\geq \frac{1}{2} \cdot 2 \Pr(i \in A) \Pr(j \in R) (\Delta_c - 2M\varepsilon)^2 \\ &\geq \alpha^2 (\Delta_c - 2M\varepsilon)^2. \end{aligned}$$

If $\alpha > 0$ and $2M\varepsilon < \Delta_c$, the right-hand side is strictly positive, ruling out collapse. \square

Remark. Theorem A.10 provides a certificate against collapse. The bound becomes vacuous only if (i) $\alpha = 0$ (low batch entropy), or (ii) $\Delta_c \leq 2M\varepsilon$ (low sharpness or prototype separation). However, as shown empirically in Appendix D.2, the model maintains high code diversity and sharpness throughout training, ensuring these conditions are met in practice.

B. Reproducibility Details

B.1. Dataset Statistics and Preprocessing

Table 5 summarizes the dataset statistics. We remove constant channels (zero variance) identified on the training split and apply the same channel mask to the test split, ensuring identical effective dimensions across splits. All remaining variables are instance-normalized independently for each window.

We construct training pairs $(\mathbf{X}_t, \mathbf{X}_{t+1})$ from two consecutive non-overlapping windows sampled from the time series. Each window has a fixed length T and is partitioned into $P=T/L$ patches with patch length $L=20$.

Table 5. **Dataset Statistics.** **Raw Dim.** is the original dimension; **Eff. Dim.** is the dimension after removing constant features.

Dataset	Raw	Eff.	Constant Indices (Zero Variance)	Train	Test	Anom (%)
MSL	55	33	[1, 4, 8, 10, 18, 21, 22, 24, 25, 26, 30, 32, 34, 36, 37, 38, 40, 42, 44, 45, 50, 51, 52]	58,317	73,729	10.5
SMAP	25	24	[16]	135,183	427,617	12.8
SWaT	51	40	[4, 10, 11, 13, 15, 29, 31, 32, 43, 48, 50]	495,000	449,919	12.1
PSM	25	25	-	132,481	87,841	27.8

B.2. Implementation Details

All methods are implemented in PyTorch and trained on a single NVIDIA GeForce RTX 4090 GPU. We use Adam for all optimizations, and unless otherwise specified, we keep the hyperparameters reported below fixed across datasets to ensure a controlled comparison. We set the latent dimension to $D=256$ and the codebook size to $K=128$, and maintain EMA target networks for both the encoder and the codebook to stabilize training.

After each optimization step on the online parameters θ , the corresponding target parameters ξ are updated by $\xi \leftarrow \rho\xi + (1 - \rho)\theta$ with decay $\rho=0.996$; gradients are not back-propagated through the EMA targets (stop-gradient).

Model Architectures.

- **Encoder:** Patch size $L=20$. The projection head is a 2-layer MLP (hidden 64→32) mapping to latent dimension $D=256$. The backbone is a 6-layer Transformer (8 heads, dropout 0.1).
- **Codebook:** Codebook size $K=128$, dimension $D=256$. Soft quantization temperature $\tau=0.1$.
- **Predictors:** Both fine and coarse predictors are 2-layer Transformers (4 heads, hidden dimension 128).

Optimization & Hyperparameters.

- **Training:** Adam optimizer ($\text{lr } 5 \times 10^{-4}$, weight decay 10^{-5}), batch size 128. Target networks are updated via EMA (decay 0.996). Gradient clipping norm is 0.5. We train for a maximum of 100 epochs, initiating model selection after 50 epochs with an early stopping patience of 10.
- **Loss Weights:** Predicted objective weights $\lambda_f=1.0$, $\lambda_c=0.5$, and $\gamma=0.1$. Codebook alignment weights $\lambda_{\text{emb}}=1.0$ and $\lambda_{\text{com}}=0.25$. Entropy regularization weights $\lambda_{\text{ent}}^{\text{sample}}=0.005$ and $\lambda_{\text{ent}}^{\text{batch}}=0.01$. Reconstruction weight λ_r is annealed linearly from 0.5 to 0.1 during training.

B.3. MTS-JEPA Pre-training Algorithm

We provide the detailed formulation of the total training objective for reproducibility. Aligning with the notation in Section 3.4, the total loss \mathcal{L} is composed of three parts:

$$\begin{aligned} \mathcal{L} = & \underbrace{\lambda_f (\mathcal{L}_{\text{KL}}^{\text{fine}} + \gamma \mathcal{L}_{\text{MSE}}^{\text{fine}}) + \lambda_c \mathcal{L}_{\text{KL}}^{\text{coarse}}}_{\text{Predictive Objective}} \\ & + \underbrace{\lambda_{\text{emb}} \mathcal{L}_{\text{emb}} + \lambda_{\text{com}} \mathcal{L}_{\text{com}} + \lambda_{\text{ent}}^{\text{sample}} \mathcal{L}_{\text{ent}}^{\text{sample}} - \lambda_{\text{ent}}^{\text{batch}} \mathcal{L}_{\text{ent}}^{\text{batch}}}_{\text{Codebook Objective}} \\ & + \underbrace{\lambda_r \mathcal{L}_{\text{rec}}}_{\text{Reconstruction}} \end{aligned}$$

Algorithm 1 summarizes the full pre-training pseudocode.

Algorithm 1 MTS-JEPA Pre-training Procedure

Require: Dataset \mathcal{D} , Online parameters θ , EMA parameters ξ , EMA rate τ

- 1: Sample batch $(\mathbf{X}_t, \mathbf{X}_{t+1}) \sim \mathcal{D}$ ▷ fine-scale future
- 2: $\mathbf{X}_{t+1}^{\text{coarse}} \leftarrow \text{Downsample}(\mathbf{X}_{t+1})$ ▷ coarse-scale future
- 3: **while** not converged **do**
- 4: $\mathbf{h}_t \leftarrow \text{Encoder}_{\theta}(\mathbf{X}_t)$ ▷ online encoding
- 5: $\mathbf{p}_t, \mathbf{z}_t \leftarrow \text{Codebook}_{\theta}(\mathbf{h}_t)$ ▷ online soft codes
- 6: $\mathcal{L}_{\text{code}} \leftarrow \text{codebook loss}$ ▷ on $(\mathbf{h}_t, \mathbf{z}_t, \mathbf{p}_t)$
- 7: $\hat{\mathbf{X}}_t \leftarrow \text{Decoder}_{\theta}(\mathbf{z}_t)$ ▷ reconstruction branch
- 8: $\mathcal{L}_{\text{rec}} \leftarrow \text{reconstruction loss}$ ▷ compare $\hat{\mathbf{X}}_t$ vs. \mathbf{X}_t
- 9: $\hat{\mathbf{p}}_{t+1}^{\text{fine}}, \hat{\mathbf{z}}_{t+1} \leftarrow \text{Predictor}_{\theta}^{\text{fine}}(\mathbf{p}_t)$ ▷ fine prediction
- 10: $\hat{\mathbf{p}}_{t+1}^{\text{coarse}} \leftarrow \text{Predictor}_{\theta}^{\text{coarse}}(\mathbf{p}_t)$ ▷ coarse prediction
- 11: $\mathbf{p}_{t+1}^{\text{fine}}, \mathbf{z}_{t+1} \leftarrow \text{EMACodebook}_{\xi}(\mathbf{X}_{t+1})$ ▷ stop-grad targets
- 12: $\mathbf{p}_{t+1}^{\text{coarse}} \leftarrow \text{EMACodebook}_{\xi}(\mathbf{X}_{t+1}^{\text{coarse}})$ ▷ stop-grad targets
- 13: $\mathcal{L}_{\text{pred}}^{\text{fine}} \leftarrow \text{prediction loss}$ ▷ $(\hat{\mathbf{p}}_{t+1}^{\text{fine}}, \hat{\mathbf{z}}_{t+1})$ vs. $(\mathbf{p}_{t+1}^{\text{fine}}, \mathbf{z}_{t+1})$
- 14: $\mathcal{L}_{\text{pred}}^{\text{coarse}} \leftarrow \text{prediction loss}$ ▷ $\hat{\mathbf{p}}_{t+1}^{\text{coarse}}$ vs. $\mathbf{p}_{t+1}^{\text{coarse}}$
- 15: $\mathcal{L}_{\text{pred}} \leftarrow \mathcal{L}_{\text{pred}}^{\text{fine}} + \mathcal{L}_{\text{pred}}^{\text{coarse}}$
- 16: $\mathcal{L}_{\text{total}} \leftarrow \mathcal{L}_{\text{pred}} + \mathcal{L}_{\text{quant}} + \lambda_r \mathcal{L}_{\text{rec}}$
- 17: Update θ ; update ξ with EMA ▷ optimizer step + EMA update
- 18: **end while**

B.4. Downstream Anomaly Prediction Protocol

Problem Formulation. We formulate the downstream task as Anomaly Prediction, distinguishing it from standard point-wise anomaly detection. The objective is to utilize a historical context window \mathbf{X}_t to predict the anomaly status of the subsequent non-overlapping future window \mathbf{X}_{t+1} . This setup evaluates the model's ability to identify early warning signs (precursors) rather than merely reacting to ongoing failures. Each dataset provides anomaly annotations as a binary indicator array aligned with the time axis, denoted by $\mathbf{a} \in \{0, 1\}^{T_{\text{full}}}$. Let \mathcal{I}_{t+1} be the set of time indices covered by the future window \mathbf{X}_{t+1} . We define the window-level label as

$$y_{t+1} = \mathbb{I}\left(\sum_{\tau \in \mathcal{I}_{t+1}} \mathbf{a}_\tau > 0\right) \in \{0, 1\}. \quad (28)$$

Let $\hat{s}_{t+1} \in [0, 1]$ denote the predicted anomaly probability and let

$$\hat{y}_{t+1} = \mathbb{I}(\hat{s}_{t+1} > \delta^*) \quad (29)$$

be the binary prediction using threshold δ^* selected on the validation set to maximize the window-level F1 score.

Notation. We denote by \mathbf{X}_t the context window and by \mathbf{X}_{t+1} the subsequent non-overlapping future window. The supervision signal is the *future-window* label $y_{t+1} \in \{0, 1\}$, which indicates whether \mathbf{X}_{t+1} is anomalous under the window-level definition above. Thus, each downstream training example is a pair (\mathbf{X}_t, y_{t+1}) , and the goal is anomaly prediction.

We report window-level Precision, Recall, and F1-score:

$$\text{Precision} = \frac{\text{TP}}{\text{TP} + \text{FP}}, \quad \text{Recall} = \frac{\text{TP}}{\text{TP} + \text{FN}}, \quad \text{F1} = \frac{2 \cdot \text{Precision} \cdot \text{Recall}}{\text{Precision} + \text{Recall}}. \quad (30)$$

We additionally report the Area Under the Receiver Operating Characteristic curve (AUC) computed from the raw probabilities \hat{s}_{t+1} .

Adaptation Strategy. We utilize the pre-trained MTS-JEPA as a frozen feature extractor. Specifically, we discard the projection heads and freeze the parameters of the encoder and codebook. For a given input \mathbf{X}_t , the encoder yields soft code probabilities $\mathbf{p}_t \in \mathbb{R}^{V \times P \times K}$, where V denotes variables, P patches, and K the codebook size. To capture the most salient anomalies across the multivariate dimensions while preserving temporal structure, we apply *Variable-wise Max-Pooling*:

$$\mathbf{h}_t = \max_{v \in \{1, \dots, V\}} \mathbf{p}_t^{(v)} \in \mathbb{R}^{P \times K}. \quad (31)$$

The aggregated representation \mathbf{h}_t is flattened and passed to an MLP classifier C_ψ , trained to estimate $\hat{s}_{t+1} = P(y_{t+1} = 1 | \mathbf{h}_t)$.

Algorithm 2 Downstream Anomaly Prediction Protocol

Require: Frozen Encoder θ , frozen Codebook, train split \mathcal{S}_{tr} , val split \mathcal{S}_{val} , test split \mathcal{S}_{te}

- 1: **Initialize** MLP classifier C_ψ
- 2: **Train:**
- 3: **for** each batch $(\mathbf{X}_t, y_{t+1}) \in \mathcal{S}_{\text{tr}}$ **do**
- 4: $\mathbf{p}_t \leftarrow \text{Codebook}(\text{Encoder}_\theta(\mathbf{X}_t))$ $\triangleright \mathbf{p}_t \in \mathbb{R}^{V \times P \times K}$
- 5: $\mathbf{h}_t \leftarrow \max_{v \in \{1, \dots, V\}} \mathbf{p}_t^{(v)}$ \triangleright variable-wise max-pooling, $\mathbf{h}_t \in \mathbb{R}^{P \times K}$
- 6: $\hat{s}_{t+1} \leftarrow C_\psi(\mathbf{h}_t)$ \triangleright anomaly probability
- 7: Update ψ using binary cross-entropy loss $\mathcal{L}_{\text{cls}}(\hat{s}_{t+1}, y_{t+1})$
- 8: **end for**
- 9: **Validate:** choose δ^* on \mathcal{S}_{val} to maximize window-level F1 using $\hat{y}_{t+1} = \mathbb{I}(\hat{s}_{t+1} > \delta)$
- 10: **Test:** report Precision/Recall/F1 on \mathcal{S}_{te} using δ^* , and AUC using raw \hat{s}_{t+1}

C. Experimental Results

C.1. Main Benchmark

Table 6 presents the comprehensive performance evaluation of our proposed method against seven baseline models across four standard anomaly detection benchmarks: MSL, SMAP, SWaT, and PSM. In addition to the F1-score and AUC reported in the main text, we provide detailed comparisons on Precision and Recall to offer a holistic view of the detection capabilities. All metrics are reported as the mean \pm standard deviation over five independent runs. The results demonstrate that our method consistently achieves superior accuracy and robustness compared to both classical unsupervised baselines (e.g., K-Means, DeepSVDD) and recent state-of-the-art multivariate time-series models (e.g., PatchTST, TS2Vec).

Table 6. Full results on four benchmark datasets. All metrics are reported in percentage (%) as mean \pm standard deviation over 5 runs with different random seeds. Best baselines are underlined.

Models	MSL				SMAP				SWaT				PSM			
	F1	AUC	Prec	Rec	F1	AUC	Prec	Rec	F1	AUC	Prec	Rec	F1	AUC	Prec	Rec
K-Means	20.63 \pm 2.30	52.17 \pm 5.65	19.27 \pm 7.16	31.34 \pm 15.40	8.74 \pm 3.39	39.82 \pm 2.57	10.52 \pm 8.17	10.16 \pm 4.92	14.45 \pm 0.38	62.20 \pm 0.16	7.99 \pm 0.32	<u>77.05</u> \pm 8.16	42.75 \pm 1.73	51.37 \pm 3.80	30.40 \pm 2.34	78.89 \pm 21.18
DeepSVDD	23.46 \pm 0.98	53.67 \pm 4.80	14.78 \pm 2.14	73.87 \pm 26.12	22.05 \pm 2.97	44.07 \pm 2.61	12.90 \pm 1.19	<u>81.99</u> \pm 24.23	15.28 \pm 1.75	58.22 \pm 2.34	12.65 \pm 1.90	20.00 \pm 3.34	44.45 \pm 1.56	49.95 \pm 3.10	30.31 \pm 3.33	89.38 \pm 16.00
LSTM-VAE	22.42 \pm 7.02	55.22 \pm 10.27	20.84 \pm 10.10	32.43 \pm 15.96	22.77 \pm 1.73	52.97 \pm 2.60	14.35 \pm 1.21	55.39 \pm 4.47	54.60 \pm 1.17	79.91 \pm 1.00	64.92 \pm 14.30	50.07 \pm 8.30	56.73 \pm 1.14	71.95 \pm 0.50	49.32 \pm 1.59	66.86 \pm 2.10
iTransformer	27.25 \pm 2.03	64.61 \pm 1.19	16.71 \pm 1.25	75.40 \pm 11.80	<u>33.00</u> \pm 2.05	60.91 \pm 1.58	22.67 \pm 2.83	64.32 \pm 10.77	70.49 \pm 1.00	82.10 \pm 0.36	<u>98.17</u> \pm 1.82	55.00 \pm 1.18	54.12 \pm 0.92	63.09 \pm 0.75	37.37 \pm 1.17	98.29 \pm 2.10
TimesNet	28.44 \pm 5.79	59.70 \pm 5.15	30.31 \pm 7.40	36.59 \pm 27.00	27.78 \pm 1.48	57.01 \pm 1.81	17.98 \pm 0.60	62.81 \pm 10.10	67.20 \pm 3.94	83.24 \pm 1.64	90.87 \pm 15.87	54.42 \pm 6.09	52.64 \pm 0.02	56.12 \pm 2.66	35.76 \pm 0.09	<u>99.71</u> \pm 0.57
PAD	21.67 \pm 0.03	55.97 \pm 6.96	12.19 \pm 0.06	<u>97.78</u> \pm 4.44	26.92 \pm 1.78	59.79 \pm 0.30	18.15 \pm 1.21	55.00 \pm 11.80	69.75 \pm 4.83	83.71 \pm 0.61	81.54 \pm 15.17	62.79 \pm 4.32	<u>57.82</u> \pm 5.96	73.84 \pm 1.85	57.54 \pm 3.18	58.57 \pm 9.17
TS-JEPA	25.49 \pm 4.22	60.33 \pm 4.65	17.10 \pm 3.91	56.84 \pm 18.65	26.57 \pm 1.67	57.38 \pm 0.72	18.23 \pm 0.74	49.73 \pm 8.05	<u>71.95</u> \pm 0.56	80.33 \pm 0.69	84.32 \pm 1.67	62.76 \pm 0.33	53.32 \pm 2.25	66.10 \pm 3.11	36.95 \pm 2.50	96.29 \pm 2.65
PatchTST	26.98 \pm 0.51	60.43 \pm 1.13	<u>75.00</u> \pm 0.00	16.45 \pm 0.38	30.06 \pm 1.20	<u>61.62</u> \pm 0.66	21.76 \pm 0.93	49.06 \pm 2.10	70.64 \pm 3.57	81.93 \pm 1.27	94.03 \pm 4.25	57.58 \pm 3.94	<u>58.17</u> \pm 0.73	<u>75.76</u> \pm 0.11	64.68 \pm 0.59	52.86 \pm 0.90
TS2Vec	23.48 \pm 2.14	<u>64.86</u> \pm 0.54	31.45 \pm 2.46	18.82 \pm 2.35	32.81 \pm 0.32	61.48 \pm 0.46	<u>23.81</u> \pm 0.30	52.81 \pm 1.95	67.00 \pm 0.83	<u>83.76</u> \pm 0.23	80.95 \pm 2.10	57.17 \pm 0.41	48.43 \pm 1.01	72.13 \pm 0.43	32.39 \pm 0.58	95.96 \pm 2.90
MTS-JEPA	<u>33.58</u> \pm 4.34	<u>66.08</u> \pm 3.25	<u>35.87</u> \pm 10.90	<u>40.80</u> \pm 15.68	<u>33.64</u> \pm 1.45	<u>65.41</u> \pm 2.06	<u>24.24</u> \pm 1.28	<u>56.02</u> \pm 8.18	<u>72.89</u> \pm 0.70	<u>84.95</u> \pm 0.82	<u>98.00</u> \pm 1.00	<u>58.05</u> \pm 1.20	<u>61.61</u> \pm 4.32	<u>77.85</u> \pm 1.28	<u>55.01</u> \pm 2.47	<u>72.00</u> \pm 12.96

C.2. Generality

We evaluate generality by comparing in-domain and cross-domain pre-training while keeping the downstream evaluation exactly the same.

For a target dataset, in-domain pre-training uses its official training set. Cross-domain pre-training uses the union of the other three datasets, with the target dataset completely excluded during pre-training. Since the source datasets may have different channel dimensions in this cross-domain setting, we treat each channel as an independent univariate series during pre-training, which avoids any explicit channel matching across datasets. After pre-training, we follow the same downstream protocol and evaluate on the same target test split in both settings, so the only difference is the source of pre-training data.

Table 7. Comparison of in-domain versus cross-domain generalization.

Models	Settings	MSL		SMAP		SWaT		PSM	
		F1	AUC	F1	AUC	F1	AUC	F1	AUC
PatchTST	In-Domain	26.98 \pm 0.51	60.43 \pm 1.13	30.06 \pm 1.20	61.62 \pm 0.66	70.64 \pm 3.57	81.93 \pm 1.27	58.17 \pm 0.73	75.76 \pm 0.11
	Cross-Domain	27.08 \pm 0.44	60.80 \pm 1.17	26.21 \pm 0.24	58.77 \pm 1.63	54.34 \pm 5.96	68.76 \pm 0.87	50.07 \pm 0.19	53.72 \pm 0.93
	Abs. Diff.	+0.10	+0.37	-3.85	-2.85	-16.30	-13.17	-8.10	-22.04
	Rel. Diff.	+0.37%	+0.61%	-12.81%	-4.63%	-23.07%	-16.07%	-13.92%	-29.09%
TS2Vec	In-Domain	23.48 \pm 2.14	64.86 \pm 0.54	32.81 \pm 0.32	61.48 \pm 0.46	67.00 \pm 0.83	83.76 \pm 0.23	48.43 \pm 1.01	72.13 \pm 0.43
	Cross-Domain	22.87 \pm 2.67	62.00 \pm 0.74	26.99 \pm 0.75	57.54 \pm 0.35	65.08 \pm 0.53	82.91 \pm 0.02	48.15 \pm 7.73	56.22 \pm 3.49
	Abs. Diff.	-0.61	-2.86	-5.82	-3.94	-1.92	-0.85	-0.28	-15.91
	Rel. Diff.	-2.60%	-4.41%	-17.74%	-6.41%	-2.87%	-1.01%	-0.58%	-22.06%
MTS-JEPA	In-Domain	33.58 \pm 4.34	66.08 \pm 3.25	33.64 \pm 1.45	65.41 \pm 2.06	72.89 \pm 0.70	84.95 \pm 0.82	61.61 \pm 4.32	77.85 \pm 1.28
	Cross-Domain	33.48 \pm 7.26	67.13 \pm 6.15	33.81 \pm 5.13	68.88 \pm 1.45	71.10 \pm 0.76	82.96 \pm 0.40	56.87 \pm 4.31	66.80 \pm 6.02
	Abs. Diff.	-0.10	+1.05	+0.17	+3.47	-1.79	-1.99	-4.74	-11.05
	Rel. Diff.	-0.30%	+1.59%	+0.51%	+5.30%	-2.46%	-2.34%	-7.69%	-14.19%

C.3. Ablation Studies

Table 8 reports the complete ablation results. All variants follow the same training and evaluation protocol as the full model, and we modify only the targeted component while keeping the rest of the architecture and training pipeline unchanged. For the codebook operation studies, the full model uses a discrete codebook bottleneck that represents each latent via soft assignment to a finite set of prototypes, with a slowly updated EMA target branch providing a stable reference for prototype states and assignment targets. To separate the effect of the bottleneck structure from the effect of auxiliary constraints, we

evaluate two complementary interventions. In the loss-only removal setting, we keep the soft codebook bottleneck in both the online and EMA target branches, and we set the auxiliary codebook regularizer weights to zero. In the module removal setting, we remove the codebook bottleneck from both branches. The model then operates purely in continuous latent space, and the predictive objective reduces to an MSE loss because the code-assignment KL term is no longer defined without discrete code distributions.

Note. When the standard deviation across random seeds is (near) zero while the mean score is low, this typically indicates model collapse, i.e., the model makes nearly identical (often single-class) predictions across runs and loses discriminative signal.

Table 8. Ablation results on four benchmark datasets.

Datasets	MSL		SMAP		SWaT		PSM	
Metrics	F1	AUC	F1	AUC	F1	AUC	F1	AUC
w/o KL Regularization	29.01 ± 6.64	53.90 ± 5.25	28.71 ± 1.71	60.19 ± 0.95	67.33 ± 3.97	79.95 ± 0.97	54.93 ± 2.54	70.83 ± 1.25
w/o Reconstruction Decoder	25.96 ± 1.82	52.68 ± 1.68	25.15 ± 0.31	52.80 ± 1.88	14.77 ± 1.42	53.30 ± 2.45	53.03 ± 0.00	69.84 ± 7.74
w/o Predictive Objective	28.88 ± 6.41	53.17 ± 1.03	27.05 ± 2.31	59.81 ± 1.76	59.47 ± 1.55	78.60 ± 0.59	58.89 ± 5.50	70.17 ± 4.73
w/o Codebook Loss	31.62 ± 1.71	58.93 ± 1.81	31.53 ± 7.88	62.06 ± 0.60	72.64 ± 1.24	82.63 ± 0.63	60.83 ± 4.09	75.85 ± 0.65
w/o Codebook Module	21.82 ± 0.00	43.02 ± 9.30	21.69 ± 0.00	51.00 ± 1.23	11.51 ± 0.00	50.00 ± 0.00	53.03 ± 0.00	46.61 ± 6.79
w/o Downsampling	28.77 ± 6.95	63.16 ± 3.83	30.39 ± 2.47	61.34 ± 0.15	71.62 ± 0.28	83.60 ± 0.40	60.79 ± 3.31	71.72 ± 4.68
Full Model	33.58 ± 4.34	66.08 ± 3.25	33.64 ± 1.45	65.41 ± 2.06	72.89 ± 0.70	84.95 ± 0.82	61.61 ± 4.32	77.85 ± 1.28

D. Visualizations and Qualitative Analysis

D.1. Framework

Figure 5 illustrates the end-to-end data flow and objectives of our framework, which consists of five coordinated components:

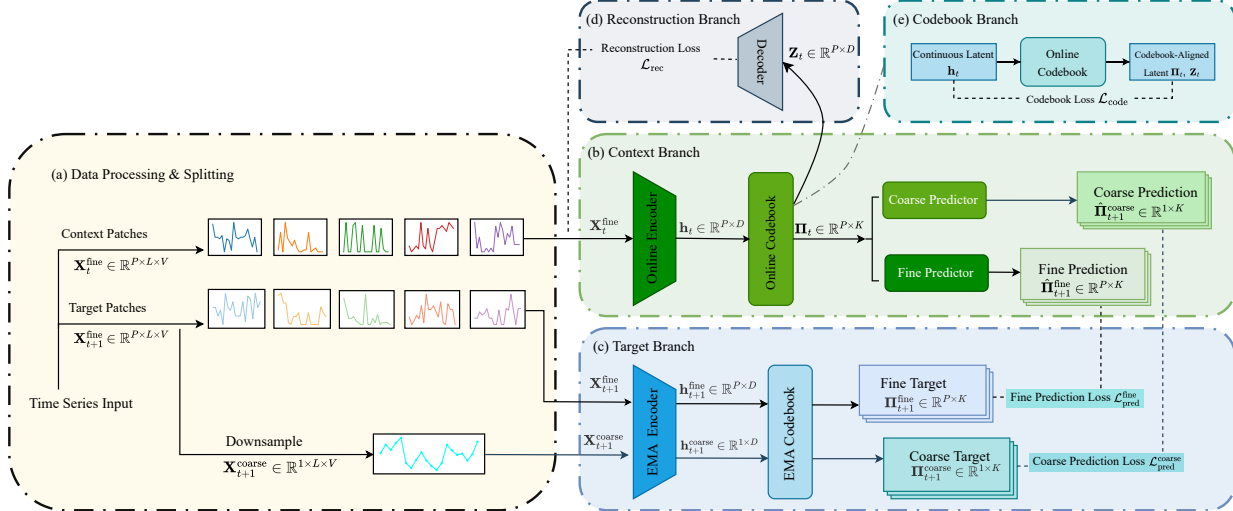


Figure 5. Overview of the Proposed Framework.

- (a) **Data Processing & Splitting:** We construct consecutive context-target pairs from non-overlapping windows. The context window is tokenized into fine-grained patches $\mathbf{X}_t^{\text{fine}} \in \mathbb{R}^{P \times L \times V}$. Simultaneously, the future window is processed into two views: fine-grained patches $\mathbf{X}_{t+1}^{\text{fine}}$ and a downsampled coarse view $\mathbf{X}_{t+1}^{\text{coarse}}$, obtained by averaging every P consecutive time points to capture low-frequency trends.
- (b) **Context Branch:** The online encoder processes the context patches $\mathbf{X}_t^{\text{fine}}$ to produce continuous latents \mathbf{h}_t . These are passed through the Online Codebook to generate the discrete code distributions $\Pi_t \in \mathbb{R}^{P \times K}$. This sequence Π_t is

then shared by two predictors: the *Fine Predictor* outputs patch-level predictions $\hat{\Pi}_{t+1}^{\text{fine}}$, while the *Coarse Predictor* aggregates the history to produce a global prediction $\hat{\Pi}_{t+1}^{\text{coarse}}$.

- (c) **Target Branch:** To provide stable supervision, the momentum-updated EMA encoder processes both future views ($\mathbf{X}_{t+1}^{\text{fine}}$ and $\mathbf{X}_{t+1}^{\text{coarse}}$). The resulting features are mapped by the EMA Codebook into target distributions Π_{t+1}^{fine} and $\Pi_{t+1}^{\text{coarse}}$. The model minimizes the prediction losses $\mathcal{L}_{\text{pred}}^{\text{fine}}$ and $\mathcal{L}_{\text{pred}}^{\text{coarse}}$ by matching the online predictions to these targets.
- (d) **Reconstruction Branch:** To prevent representation collapse and anchor the semantics, a decoder reconstructs the original signal from the codebook-aligned embeddings \mathbf{Z}_t , optimizing the reconstruction loss \mathcal{L}_{rec} .
- (e) **Codebook Branch:** This module aligns the continuous latents \mathbf{h}_t with the discrete code assignments Π_t and embeddings \mathbf{Z}_t . It computes the codebook loss $\mathcal{L}_{\text{code}}$, which regularizes the assignment probabilities to ensure the codebook remains utilized and structured.

D.2. Latent Code Analysis

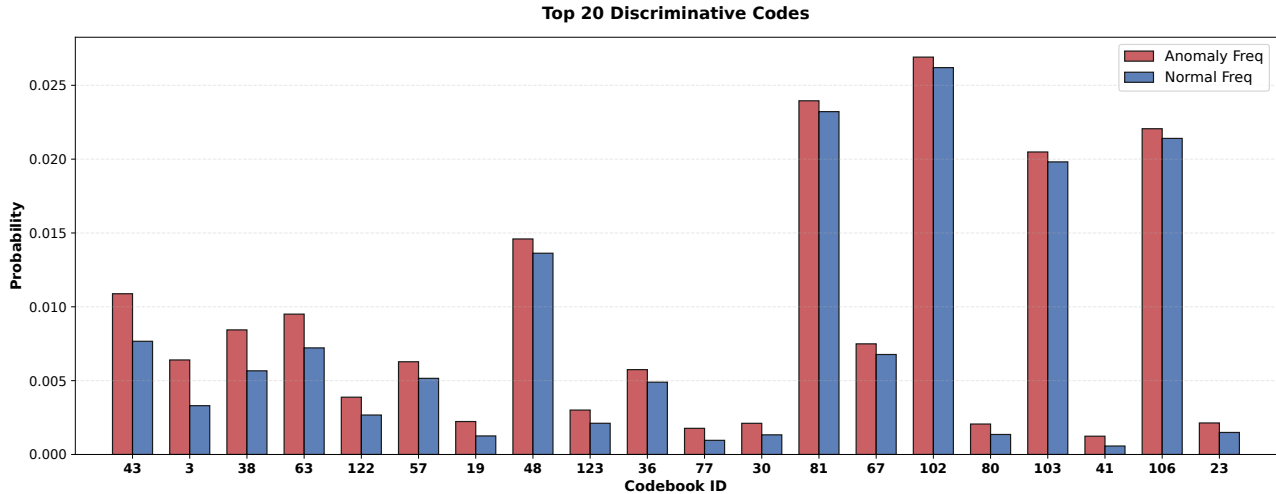


Figure 6. Histogram comparing the occurrence probability of latent codes in anomalous versus normal windows on the PSM test set.

To interpret the semantic structure of the learned latent space, Figure 6 visualizes the activation probability of codebook entries on the PSM dataset, which was selected for its challenging high-dimensional real-world server telemetry. The codebook entries are arranged from left to right based on the magnitude of the frequency discrepancy between anomalous and normal windows, meaning that the codes on the far left exhibit the greatest distinction between the two states. This sorting highlights that specific latent codes act as highly discriminative structural prototypes which are disproportionately active during anomalies, confirming that the model extracts robust and interpretable signals indicative of system health rather than utilizing the codebook uniformly.

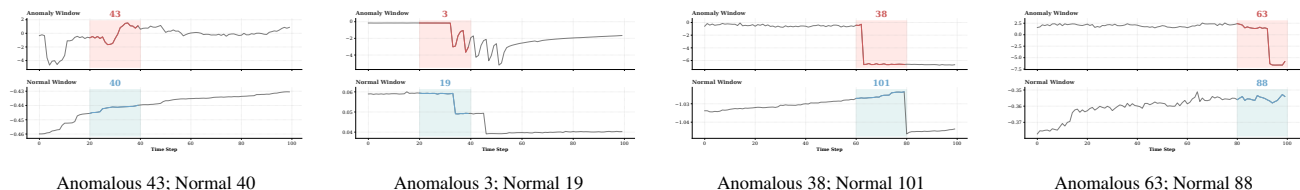


Figure 7. Window-level comparisons of dominant latent codes between anomalous and normal windows on the PSM dataset. Shaded regions indicate patch-level segments where the dominant code is selected.

Figure 7 maps the most discriminative latent codes back to their corresponding time-series patches to validate the benefits of the discrete bottleneck. The distinct morphological differences observed between anomalous prototypes (e.g., Code 43)

and their normal counterparts illustrate how the codebook acts as a regularizer: by suppressing minor nuisance variations, it forces the model to capture stable structural motifs. This confirms that our approach effectively disentangles precursor-like patterns from routine dynamics, establishing a robust and interpretable basis for anomaly prediction.

D.3. Inference Efficiency

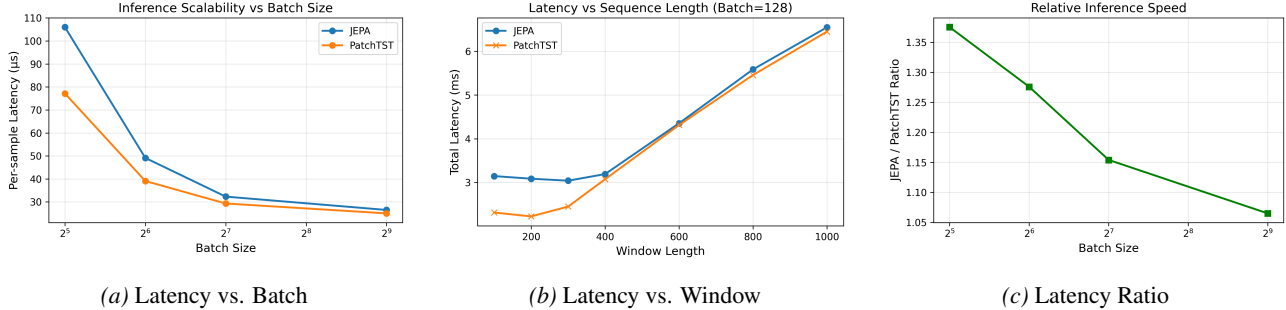


Figure 8. Inference-time scaling comparisons across batch size, window length, and latency ratios.

Figure 8 evaluates the inference efficiency of MTS-JEPA compared with PatchTST from three complementary perspectives. First, Figure 8a reports the per-sample latency vs. batch size: MTS-JEPA is slower, but the gap shrinks at larger batches. Figure 8b then reports latency vs. window length (batch fixed): both scale similarly, with MTS-JEPA slightly slower. Figure 8c confirms this trend: the latency ratio decreases as batch size increases.

Overall, these results highlight a limitation of our approach: inference efficiency is not a primary contribution of MTS-JEPA, as its richer architecture incurs higher computational cost than a single-backbone baseline. Our design instead prioritizes early-warning performance and representation stability, with the runtime overhead becoming more manageable in deployment scenarios that support moderate to large batch sizes.